Resummed Perturbation Theory of Galaxy Clustering

Xin Wang* and Alex Szalay
Department of Physics and Astronomy, Johns Hopkins University, Baltimore, MD 21218, US
(Dated: February 7, 2022)

The relationship between observed tracers such as galaxies and the underlying dark matter distribution is crucial in extracting cosmological information. As the linear bias model breaks down at quasi-linear scales, the standard perturbative approach of the nonlinear Eulerian bias model (EBM) is not accurate enough in describing galaxy clustering. In this paper, we discuss such a model in the context of resummed perturbation theory, and further generalize it to incorporate the subsequent gravitational evolution by combining with a Lagrangian description of galaxies' motion. The multipoint propagators we constructed for such model also exhibit exponential damping similar to their dark matter counterparts, therefore the convergence property of statistics built upon these quantities is improved. This is achieved by applying both Eulerian and Lagrangian resummation techniques of dark matter field developed in recent years. As inherited from the Lagrangian description of galaxy density evolution, our approach automatically incorporates the non-locality induced by gravitational evolution after the formation of the tracer, and also allows us to include a continuous galaxy formation history by temporally weighted-averaging relevant quantities with the galaxy formation rate.

arXiv:1204.0019v1 [astro-ph.CO] 30 Mar 2012

I. INTRODUCTION

Large-scale structure surveys provide a wealth of cosmological information in probing dark energy, modified gravity, neutrino masses and the physics of early universe. As the statistical uncertainty decreases dramatically in next generation surveys, it requires us to achieve an unprecedented level of accuracy in theoretically predicting the statistics of the observed clustering pattern. Since nonlinear dynamics plays a important role in understanding the observed data in relevant regime, it has attracted lots of interest in developing the nonlinear perturbation theory of the dark matter beyond the standard approach. Many sophisticated methods have been proposed, including the renormalized perturbation theory (RPT) [1–3], the Lagrangian resummation theory [4], the closure theory [5], and the time renormalization group theory (TRG) [6]. However, the relationship between various observable tracers (galaxies, quasars, Lyα forest, clusters and HI galaxies etc.) and the underlying dark matter field may be more challenging. The linear bias model breaks down even for present surveys [7, 8] at relatively large scale, the scale-dependence observed in the data varies among different galaxy samples as one would expect [7], and the empirical fitting formula [9] widely used in the data analysis is not able to describe such differences among samples and eventually leads to inconsistent cosmological constraints [7].

Two different approaches exist in modeling the scale-dependent bias of galaxies these days. One is the halo-based model which starts from the large scale clustering of dark matter halos and then populates with different types of galaxies according to the halo occupation distribution (HOD) function. The other approach is the perturbative bias model, which packs the complicated baryonic physics into a general unknown functional depending on the dark matter distribution, and characterize it with the first few bias parameters. With a careful parameterized and calibrated HOD function, the first approach can describe the two-point statistics qualitatively well at small scale. However, a viable HOD parameterization usually contains lots of free parameters, and heavily depends on calibration from simulation. Moreover, in the quasi-linear regime where most of large-scale surveys probe, the accuracy of such approach is usually not satisfactory.

On the other hand, the standard perturbative bias model is also problematic. In the Eulerian bias model (EBM), the observed galaxy number density depends on the Eulerian dark matter distribution at the time of observation. Therefore, this model breaks down as the dark matter perturbations evolve into the nonlinear regime at small scales and later times. Since both the large-scale amplitude and small-scale shape of the power spectrum depend on higher-order bias parameters, such calculation would fail within the whole range of scales. Furthermore, although adopting some artificial nonlocal bias parameters won't bring too much intrinsic difficulties in the calculation, most authors simply assume that the functional form of the galaxy density only depends on the matter distribution locally, which is not consistent with the nonlocal gravitational evolution of the tracer [10, 11].

Since the difficulties of the perturbative convergence encountered in the nonlinear bias model is very similar to the situation in dark matter field, one would expect to generalize any of previous nonstandard matter perturbation theory to describe the clustering of biased tracer. Several works have already been done along this direction. In [12], a Lagrangian bias model (LBM) which intended to incorporate the halo bias and redshift distortion was proposed based on a similar resummation theory for matter distribution [4]. Then [13] also included

*Electronic address: wangxin@pha.jhu.edu

the halo bias in the time renormalization group methods. [14, 15] approached in a different way by redefining the bias parameters. As we will show in this paper, with the help of recent development in the renormalized perturbation theory [1–3], it is also possible to construct a resummed perturbation theory for nonlinear Eulerian bias model, and the perturbative expansion of statistics can be rewritten through the so-called $\Gamma-$expansion, first introduced by [3], with the building blocks known as multipoint propagators. One advantage of the $\Gamma-$expansion is that for Gaussian initial conditions, all contributions are positive and centralized within a limited range of scale. As we will see later, such an expansion is quite general and applicable to many circumstances as long as the multipoint propagators can be well estimated. Therefore in the following, this paper will mainly concentrate on constructing the multipoint propagators for various objects. The validity of such technique has already been verified in calculating the power spectrum of logarithmic mapping of the density field [16]. It have been shown that even for the slow converging function such as logarithm, the calculation agrees with the simulation quite well.

We further generalize the Eulerian bias model by separating the complicated nonlinear physical processes during the galaxy formation and the subsequent gravitational evolution until been observed by a survey. As we will show, this can be achieved by combining the Eulerian bias model and Lagrangian description of galaxy motion introduced in [12]. Like EBM, we assume the galaxy distribution created at some time is characterized by a general unknown functional, and the galaxy number density observed at a Eulerian position later can be naturally described by the Lagrangian version of continuity equation. Consequently, this approach also enables us to incorporate continuous galaxy formation by temporally averaging the distribution of newborn galaxies weighted with the galaxy formation rate. In such a framework, while the complex galaxy formation physics is simplified by a few bias parameters, we are able to capture the following gravitational evolution after its creation, which would in principal induce non-locality and can not be accurately described by a local Eulerian bias model. As inherited from the Lagrangian bias model and our resumed calculation of Eulerian bias model, this model can also be expressed in a resummed manner.

In section II, we briefly review both Eulerian and Lagrangian perturbation theory of dark matter field, including both standard approach and resummed theory. We will also introduce the concept of the multipoint propagator in the context of Lagrangian perturbation theory, and give a explicit calculation in Appendix A. In section III, we first review the standard Eulerian and Lagrangian bias model, and then introduce our continuous galaxy formation model. We construct the resummed Eulerian bias model in Section IV, and the generalize it in Section V. Finally, we conclude in Section VI.

II. PERTURBATION THEORY OF DARK MATTER

In this section, we will briefly review both Eulerian perturbation theory (EPT) and the Lagrangian perturbation theory (LPT) of the dark matter field, including both the standard approach and resummed calculation.

A. Dynamical Equation of Motion

The gravitational dynamics of a pressureless fluid before shell crossing is governed by the continuity, Euler, and Poisson equations.

$$\begin{aligned}
&\frac{\partial\delta(\mathbf{x},\tau)}{\partial\tau}+\nabla\cdot\left[\ \big(1+\delta(\mathbf{x},\tau)\big)\ \mathbf{u}(\mathbf{x},\tau)\ \right]=0,\\
&\frac{\partial\mathbf{u}(\mathbf{x},\tau)}{\partial\tau}+\mathcal{H}(\tau)\mathbf{u}(\mathbf{x},\tau)+\mathbf{u}(\mathbf{x},\tau)\cdot\nabla\mathbf{u}(\mathbf{x},\tau)\\
&\qquad\qquad\qquad\qquad=-\nabla\Phi_N(\mathbf{x},\tau)\\
&\nabla^2\Phi_N(\mathbf{x},\tau)=\frac{3}{2}\Omega_m(\tau)\mathcal{H}^2(\tau)\delta(\mathbf{x},\tau).
\end{aligned}\tag{1}$$

Here, $\mathcal{H}=d\ln a(\tau)/d\ln\tau$ is the Hubble expansion rate, $a(\tau)$ is the scale factor, $\Omega_m(\tau)$ is the ratio of matter density to critical density, and $\Phi_N(\mathbf{x},\tau)$ is the Newtonian potential.

Following [1, 2], the equation of motion in Fourier space can be written in a compact form by defining the two-component variable

$$\mathbf{\Xi}_a(\mathbf{k},\eta)=\big(\delta(\mathbf{k},\eta),\ \ -\theta(\mathbf{k},\eta)/\mathcal{H}\big),\tag{2}$$

where θ denotes the divergence of peculiar velocity $\nabla\cdot\mathbf{u}$. The index $a\in\{1,2\}$ stands for matter density or velocity variables, respectively. In the following, we will interchangeably use Ξ_1, Ξ_m and δ_m for matter overdensity, while using both Ξ_g and δ_g for galaxy perturbation.

The equation of motion then reads

$$\begin{aligned}
\partial_\eta\mathbf{\Xi}_a(\mathbf{k},\eta)\ &+\ \Omega_{ab}\mathbf{\Xi}_b(\mathbf{k},\eta)\\
&=\ \gamma_{abc}(\mathbf{k},\mathbf{k}_1,\mathbf{k}_2)\mathbf{\Xi}_b(\mathbf{k}_1,\eta)\mathbf{\Xi}_c(\mathbf{k}_2,\eta),
\end{aligned}\tag{3}$$

with the convention that repeated Fourier arguments are integrated over. The time $\eta=\ln a(\tau)$ in a Einstein-de Sitter (EdS) universe. Here the constant matrix

$$\Omega_{ab}=\begin{bmatrix}0 & -1\\ -3/2 & 1/2\end{bmatrix},\tag{4}$$

derived for an EdS universe, is still applicable in other cosmologies with negligible corrections to the coefficients, using $\eta=\ln D(\tau)$ (with D the linear growth factor).

The symmetrized vertex matrix γ_{abc} is given by

$$\begin{aligned}
\gamma_{222}(\mathbf{k},\mathbf{k}_1,\mathbf{k}_2)\ &=\ \delta_D(\mathbf{k}-\mathbf{k}_1-\mathbf{k}_2)\frac{|\mathbf{k}_1+\mathbf{k}_2|^2(\mathbf{k}_1\cdot\mathbf{k}_2)}{2k_1^2k_2^2}\\
\gamma_{121}(\mathbf{k},\mathbf{k}_1,\mathbf{k}_2)\ &=\ \delta_D(\mathbf{k}-\mathbf{k}_1-\mathbf{k}_2)\frac{(\mathbf{k}_1+\mathbf{k}_2)\cdot\mathbf{k}_1}{2k_1^2}
\end{aligned}\tag{5}$$

$\gamma_{112}(\mathbf{k},\mathbf{k}_1,\mathbf{k}_2)=\gamma_{121}(\mathbf{k},\mathbf{k}_2,\mathbf{k}_1)$, and $\gamma=0$ otherwise.

Then the formal integral solution to Eq. (3) can be derived as

$$\begin{aligned}\boldsymbol{\Xi}_a(\mathbf{k},\eta) &= g_{ab}(\eta)\phi_b(\mathbf{k})+\int_0^\eta d\eta'\ g_{ab}(\eta-\eta')\\ &\times\gamma_{bcd}(\mathbf{k},\mathbf{k}_1,\mathbf{k}_2)\boldsymbol{\Xi}_c(\mathbf{k}_1,\eta')\boldsymbol{\Xi}_d(\mathbf{k}_2,\eta')\end{aligned}\quad(6)$$

where $\phi_a(\mathbf{k})$ denotes the initial condition $\phi_a(\mathbf{k})\equiv\Xi_a(\mathbf{k},\eta=0)$, and the linear propagator $g_{ab}(\eta)$ is given by

$$g_{ab}(\eta)=\frac{e^\eta}{5}\begin{bmatrix}3&2\\3&2\end{bmatrix}-\frac{e^{-3\eta/2}}{5}\begin{bmatrix}-2&2\\3&-3\end{bmatrix}.\quad(7)$$

In the following, we adopt growing-mode initial conditions $\phi_a(\mathbf{k})=\delta_0(\mathbf{k})u_a$, with $u_a=(1,1)$.

In Lagrangian perspective, the dynamic of a fluid element at initial Lagrangian position $\mathbf{q}$ is entirely described by the final Eulerian position $\mathbf{x}$, or equivalently the displacement field $\boldsymbol{\Psi}(\mathbf{q})=\mathbf{x}-\mathbf{q}$, which is governed by the equation of motion,

$$\frac{d^2}{d\tau^2}\boldsymbol{\Psi}+\mathcal{H}(\tau)\frac{d}{d\tau}\boldsymbol{\Psi}=-\nabla\Phi_N\quad(8)$$

where ∇ is still the derivative with respect to Eulerian coordinates $\mathbf{x}$, and the gravitational potential Φ_N is determined by Poisson equation as shown in Eq. (1). The density contrast is then related to $\boldsymbol{\Psi}(\mathbf{q})$ via mass conservation

$$1+\delta_m(\mathbf{x})=J^{-1}=\Big[\det\left[\delta_{ij}+\Psi_{i,j}(\mathbf{q})\right]\Big]^{-1}\quad(9)$$

where J is the Jacobian of the transformation between Eulerian and Lagrangian space, and $\Psi_{i,j}=\partial\Psi_i/\partial q_j$. To linear order, Eq. (8) is then solved by the Zel'dovich approximation $\nabla_q\cdot\boldsymbol{\Psi}^{(1)}(\mathbf{q})=-D(\tau)\delta_0(\mathbf{q})$, with Lagrangian derivative ∇_q.

B. Eulerian Perturbation Theory

A perturbative solution to Eq. (6) could be obtained by expanding in terms of initial fields

$$\begin{aligned}\boldsymbol{\Xi}_a(\mathbf{k},\eta) &= \sum_{n=1}^{\infty}\boldsymbol{\Xi}_a^{(n)}(\mathbf{k},\eta)\\ \boldsymbol{\Xi}_a^{(n)}(\mathbf{k},\eta) &= \int d^3\mathbf{q}_{1\cdots n}\ \delta_D(\mathbf{k}-\mathbf{q}_{1\cdots n})\mathcal{F}^{(n)}_{ab_1\cdots b_n}(\mathbf{q}_1,\cdots,\\ &\cdots,\mathbf{q}_n;\eta)\phi_{b_1}(\mathbf{q}_1)\cdots\phi_{b_n}(\mathbf{q}_n)\end{aligned}\quad(10)$$

where $d^3\mathbf{q}_{1\cdots n}$ is short for $d^3\mathbf{q}_1\cdots d^3\mathbf{q}_n$, and $\mathbf{q}_{1\cdots n}$ denotes $\mathbf{q}_1+\cdots+\mathbf{q}_n$. The kernels $\mathcal{F}^{(n)}$ are fully symmetric functions of the wave vectors. As shown in [2], they can be obtained in terms of g_{ab} and γ_{abc} recursively.

$$\begin{aligned}&\mathcal{F}_a^{(n)}(\mathbf{k}_1,\cdots,\mathbf{k}_n;\eta)\delta_D(\mathbf{k}-\mathbf{k}_{1\cdots n})=\\ &\Big[\textstyle\sum_{m=1}^n\int_0^\eta d\eta' g_{ab}(\eta-\eta')\ \gamma_{bcd}(\mathbf{k},\mathbf{k}_{1\cdots m},\mathbf{k}_{m+1\cdots n})\\ &\times\ \mathcal{F}_c^{(m)}(\mathbf{k}_{1\cdots m};\eta')\ \mathcal{F}_c^{(n-m)}(\mathbf{k}_{m+1\cdots n};\eta')\Big]_{\text{symmetrized}}\end{aligned}\quad(11)$$

For $n=1$, $\mathcal{F}_a^{(1)}(\eta)=g_{ab}(\eta)u_b$. It should be noted that in this formalism, the kernel depends on the time η, since it includes subleading terms in e^η [1]. If one only considers the fastest-growing mode, $\mathcal{F}_a^{(n)}(\eta)$ equals the well-known PT kernel $D^n(\eta)\{F^{(n)},G^{(n)}\}$, where $D(\eta)$ is the linear growth factor.

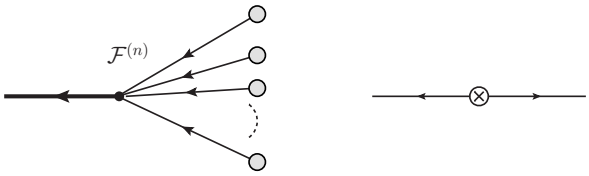

FIG. 1: Diagrammatic elements of Eulerian perturbation theory. *left*: perturbative expansion (Eq. 10); *right*: initial power spectrum $P_0(k)$.

The power spectrum $P_m(k,\eta)$ of the matter density perturbation is defined as

$$P_m(k,\eta)\delta_D(\mathbf{k}+\mathbf{k}')=\langle\Xi_m(\mathbf{k},\eta)\ \Xi_m(\mathbf{k}',\eta)\rangle\quad(12)$$

For Gaussian initial conditions, all the statistical information is encoded in the initial power spectrum

$$\langle\phi_a(\mathbf{k})\phi_b(\mathbf{k}')\rangle=\delta_D(\mathbf{k}+\mathbf{k}')P_{ab}(k),\quad(13)$$

where $P_{ab}(k)=u_au_bP_0(k)$, with $P_0(k)=\langle\delta_0(\mathbf{k})\delta_0(\mathbf{k}')\rangle$. Diagrammatically, as shown in the right-hand diagram of Fig. (1), the ensemble average is obtained by gluing two open circles together to form the symbol $\otimes$, which represents the initial power spectrum $P_{ab}(k)$.

As the density fluctuations evolve into the non-linear regime at later times, the validity of standard perturbation theory breaks down, loop contributions become ill-behaved and the convergence of perturbation series gets out of control. As one of several different approaches beyond SPT been proposed recently, we will briefly review the renormalized perturbation theory (RPT) introduced by [1–3], and then the Lagrangian resummation theory [4] in the next subsection.

The crucial step of renormalized perturbation theory is to define the generalized growth factor, known as the propagator $\Gamma^{(1)}_{m\ ab}(k)$

$$\Gamma^{(1)}_{m\ ab}(k,\eta)\delta_D(\mathbf{k}-\mathbf{k}')\equiv\left\langle\frac{\delta\Xi_a(\mathbf{k},\eta)}{\delta\phi_b(\mathbf{k}')}\right\rangle,\quad(14)$$

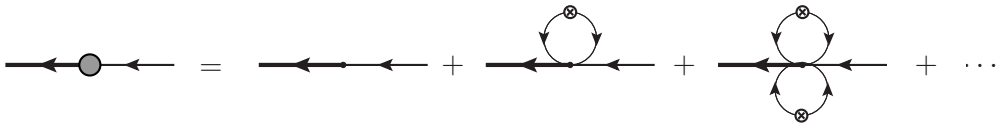

FIG. 2: The nonlinear propagator $\Gamma^{(1)}_m(k,\eta)$ has an infinite number of loop contributions.

which effectively describes the time evolution of individual Fourier modes when non-linear mode-coupling is included. Here δ denotes the functional derivative. The propagator measures the dependence of a non-linearly evolved Fourier mode $\Xi_a(\mathbf{k},\eta)$ on its initial state $\phi_b(\mathbf{k})$ on average. Intuitively, one should expect G_{ab} to decay to zero at small scales since non-linear mode-coupling has erased all the information from the initial state at that $\mathbf{k}$. Indeed, with the help of the Feynman diagrams introduced in [1], the dominant contribution can be summed up explicitly in the large-k limit, and giving the exponential decay $G_{ab}(k) \approx \exp(-k^2D^2\sigma^2_\Psi/2)$. In this paper, the non-linear propagator is diagrammatically presented as a grey circle with an incoming branch. It is a summation of infinite number of loop contributions, as illustrated in Fig. (2).

Given above, [1] was able to rewrite the nonlinear matter density power spectrum as a sum of two contributions

$$P_m(k,\eta) = G^2(k,\eta)P_0(k) + P_{MC}(k,\eta), \tag{15}$$

where G is the density propagator $G(k,\eta) = G_{1b}u_b$, and $P_{MC}(k,\eta)$ is the mode-coupling term. Therefore, the non-linear power spectrum at any $\mathbf{k}$ is composed of two parts. One is proportional to the initial power spectrum at the same $\mathbf{k}$; the other comes from mode-coupling of other $\mathbf{k}'$. As $G(k)$ decays at small scales, more and more power comes from the mode-coupling contribution. [3] showed that these complicated mode-coupling contributions can be expressed as a summation of multi-point propagators, defined as

$$\begin{aligned}\Gamma^{(n)}_{m\ ab_1\cdots b_n}(\mathbf{k}_1,\cdots,\mathbf{k}_n;\eta)\delta_D(\mathbf{k}-\mathbf{k}_{1\cdots n}) \\ = \quad \frac{1}{n!}\left\langle \frac{\delta^n \Xi_a(\mathbf{k},\eta)}{\delta\phi_{b_1}(\mathbf{k}_1)\cdots\delta\phi_{b_n}(\mathbf{k}_n)}\right\rangle,\end{aligned} \tag{16}$$

which is nothing but a generalization of two-point propagator G_{ab}. Similarly, the dominant part of multi-point propagators can also be summed and decay into the nonlinear regime at the same rate as two-point propagator. [3] showed that a simple approximation which generalizes the k-dependence of two-point propagators agrees with the data with acceptable accuracy,

$$\begin{aligned}\Gamma^{(n)}_m(\mathbf{k}_1,\cdots,\mathbf{k}_n;\eta) \ &= \ \Gamma^{(n,\ \mathrm{tree})}_m(\mathbf{k}_1,\cdots,\mathbf{k}_n;\eta) \\ &\times \ \frac{\Gamma^{(1)}_m(|\mathbf{k}_{1\cdots n}|)}{\Gamma^{(1,\ \mathrm{tree})}_m(|\mathbf{k}_{1\cdots n}|)}.\end{aligned} \tag{17}$$

For gaussian initial condition, the nonlinear power spectrum can then be expressed with the help of Eq.(16), known as the $\Gamma-$expansion

$$\begin{aligned}P_{m\ ab}(k,\eta) \ &= \ \sum_{n\geq 1} n! \int d^3\mathbf{q}_{1\cdots n}\ \delta_D(\mathbf{k}-\mathbf{q}_{1\cdots n}) \\ &\Gamma^{(n)}_{m\ a}(\mathbf{q}_1,\cdots,\mathbf{q}_n;\eta)\ \Gamma^{(n)}_{m\ b}(\mathbf{q}_1,\cdots,\mathbf{q}_n;\eta) \\ &P_0(q_1)\cdots P_0(q_n).\end{aligned} \tag{18}$$

Note that Eq. (18) describes nothing but an alternative way of taking ensemble averages, or diagrammatic speaking, gluing initial states. Instead of gluing two density fields order by order, one can first construct the objects by gluing initial states of individual density fields with n incoming branches, known as an $(n+1)$-point propagator, and the final non-linear power spectrum is then obtained by gluing two propagators together. Therefore, this $\Gamma-$expansion is quite general and applicable to the ensemble average of any two arbitrary statistical fields $\langle x_1 x_2\rangle$, which are functionals of some other field x_0

$$\begin{aligned}x_i[x_0(\mathbf{k}_n),\lambda] \ &= \ \sum_n \int d^3\mathbf{k}_{1\cdots n}\ X^{(n)}_i(\mathbf{k}_1,\cdots,\mathbf{k}_n;\lambda) \\ &\times\ [x_0(\mathbf{k}_1)\cdots x_0(\mathbf{k}_n)],\end{aligned} \tag{19}$$

as long as the building blocks are well estimated. Here λ symbolize some parameters, and $X^{(n)}$ are symmetric on their arguments. In the case that x_0 is Gaussian, the Wick's theorem ensures that the ensemble average of an odd number of fields vanishes $\langle x_0(1)\cdots x_0(2n+1)\rangle = 0$ and the average of an even number of fields $\langle x_0(1)\cdots x_0(2n)\rangle$ can be decomposed as summation of two-point correlations

$$\langle x_0(1)\cdots x_0(2n)\rangle = \sum_{\text{all pairs}}\prod_{ij}\langle x_0(i)x_0(j)\rangle. \tag{20}$$

Following the idea of [3], there are three types of two-point correlations $\langle x_0(i)x_0(j)\rangle$ involved in calculating $\langle x_1(\lambda)x_2(\lambda')\rangle$: pairs within x_1 or x_2 themselves and pairs connecting them. Therefore, one is always able to regroup Eq.(20) in the following way

$$\begin{aligned}\langle x_0(1)\cdots x_0(2n)\rangle = \sum_{\text{in between}}\Bigg[\sum_{x_1\ \text{internal}}\prod_{lm}\langle x_0(l)x_0(m)\rangle\Bigg] \\ \Bigg[\sum_{x_2\ \text{internal}}\prod_{l'm'}\langle x_0(l')x_0(m')\rangle\Bigg]\Bigg[\prod_{ij\ \text{in between}}\langle x_0(i)x_0(j)\rangle\Bigg].\end{aligned} \tag{21}$$

Combining above equations (19, 20 and 21) together, one is able to reformulate $\langle x_1(\lambda)x_2(\lambda')\rangle$ as a sum of two-point cross correlations of x_0 belonging to x_1 and x_2 respectively with some pre-summed nonlinear quantity involving internal pairs $\sum_{\rm internal}\prod_{lm}\langle x_0(l)x_0(m)\rangle$, which can be formally defined as the average of functional derivative

$$\Gamma_i^{(n)} = \frac{1}{n!}\left\langle \frac{\delta^n x_i}{\delta x_0(1)\cdots\delta x_0(n)}\right\rangle. \tag{22}$$

Therefore, as long as $\Gamma_i^{(n)}$ is well estimated, one is always able to carry out the $\Gamma-$expansion in such situation. In the following, we will demonstrate that with the help of the density propagator of cold dark matter (Eq. 16), many similar quantities of this kind can be calculated. And we will extensively utilize such expansion in the following of the paper.

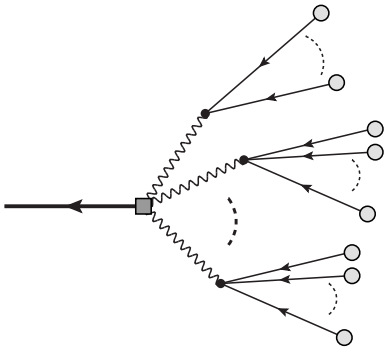

FIG. 3: Diagrammatic representation of nonlinear matter density perturbation in Lagrangian perturbation theory, similar to the one introduced in [4]. The wavy line denotes the displacement field $\mathbf{\Psi}$, and the thin solid lines together with grey open circles stand for the linear density perturbations δ_0.

C. Lagrangian Perturbation Theory

As discussed in the beginning of this section, the dynamics of the system in Lagrangian picture is fully characterized by the displacement field $\mathbf{\Psi}(\mathbf{q},\eta)$. Combining the equation of motion (Eq. 8) and the Poisson equation, the displacement field can be solved perturbatively. In Fourier space, the $n-$th order perturbation $\mathbf{\Psi}^{(n)}$ can be generally expressed as

$$\mathbf{\Psi}^{(n)}(\mathbf{k}) = \frac{iD^n}{n!}\int d^3\mathbf{p}_{1\cdots n}\ \mathbf{L}^{(n)}(\mathbf{p}_{1\cdots n})\delta_0(\mathbf{p}_1)\cdots\delta_0(\mathbf{p}_n), \tag{23}$$

where $\mathbf{L}^{(n)}$ is the perturbation kernel.

Due to the matter conservation, the Eulerian density contrast $\delta_m(\mathbf{x})$ can be expressed as

$$1+\delta_m(\mathbf{x}) = \int d^3\mathbf{q}\,[1+\delta_0(\mathbf{q})]\,\delta_D(\mathbf{x}-\mathbf{q}-\mathbf{\Psi}(\mathbf{q})). \tag{24}$$

For the matter distribution, one usually assumes that the initial field is sufficiently uniform $\delta_0\approx 0$, so that above equation (Eq. 24) can be further simplified. In Fourier space,

$$\begin{aligned}\delta_m(\mathbf{k}) &= \int d^3\mathbf{q}\ e^{-i\mathbf{k}\cdot\mathbf{q}}\ \left[e^{-i\mathbf{k}\cdot\mathbf{\Psi}(\mathbf{q})}-1\right]\\ &= \sum_{n=1}^{\infty}\frac{(-i)^n}{n!}\int d^3\mathbf{p}_{1\cdots n}\,[\mathbf{k}\cdot\mathbf{\Psi}(\mathbf{p}_1)]\cdots[\mathbf{k}\cdot\mathbf{\Psi}(\mathbf{p}_n)]\\ &\qquad\times\ \delta_D(\mathbf{k}-\mathbf{p}_{1\cdots n}).\end{aligned} \tag{25}$$

Similarly, the above equation can also be represented by diagrams as shown in Fig. (3). Here, wavy lines denote the displacement field $\mathbf{\Psi}$, and the thin solid line together with grey open circle stands for the linear density perturbation, i.e. Eq.(23).

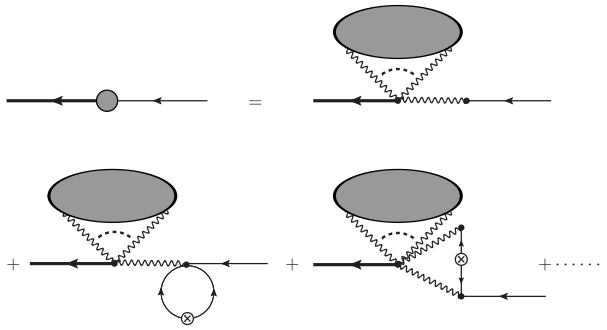

FIG. 4: Two-point propagator of matter density $\Gamma_m^{(1)}(\mathbf{k})$ in the context of Lagrangian perturbation theory up to one-loop order. The grey ellipse shown in each contribution symbolizes the quantity of Eq (26). Note here we have omitted the summation sign over the displacement field $\mathbf{\Psi}$ presented in [10].

Starting from Eq.(25), [4] performed a resummation of the power spectrum of the density contrast, known as Lagrangian Resummed Perturbation Theory. Although not been explicitly discussed in [4], it is also possible to define the same propagator within this framework. First of all, as pointed out in [10] for biased tracers[1], the following quantity can be resummed

$$\begin{aligned}&\sum_{n=0}^{\infty}\frac{(-i)^n}{n!}\int d^3\mathbf{p}_{1\cdots n}\ [k_{i_1}\cdots k_{i_n}]\,\langle\Psi_{i_1}(\mathbf{p}_1)\cdots\Psi_{i_n}(\mathbf{p}_n)\rangle\\ &=\sum_{n=0}^{\infty}\frac{(-i)^n}{n!}\left\langle\left[\int d^3\mathbf{p}\ \mathbf{k}\cdot\mathbf{\Psi}(\mathbf{p})\right]^n\right\rangle = \langle e^{-i\mathbf{k}\cdot\mathbf{\Psi}(0)}\rangle,\end{aligned} \tag{26}$$

where $\mathbf{\Psi}(0)=\int d^3\mathbf{p}\ \mathbf{\Psi}(p)$ is the displacement field at the origin. It is represented as a grey ellipse in Fig. (4), and

[1] Setting $b_1=1$ and $b_n=0$ otherwise in Eq. (71) of [10], one recovers the following equation.

can be further simplified as [4, 10]

$$\begin{aligned}\left\langle e^{-i\mathbf{k}\cdot\mathbf{\Psi}(0)}\right\rangle &= \Pi^{(0)}(\mathbf{k}) = \exp\left[\left\langle e^{-i\mathbf{k}\cdot\mathbf{\Psi}(0)}\right\rangle_c\right] \\ &= \exp\left[\sum_{n=1}^{\infty}\frac{(-1)^n\langle|\mathbf{\Psi}(0)|^{2n}\rangle_c}{(2n+1)(2n)!}k^{2n}\right] \\ &\approx \exp\left[-\frac{k^2D^2}{2}\sigma_\Psi^2\right] \end{aligned} \quad (27)$$

with the variance of displacement field along one direction $D^2\sigma_\Psi^2 = \langle|\mathbf{\Psi}(0)|^2\rangle/3 = \int d^3\mathbf{q}D^2P_0(q)/(3q^2)$. Here, we have used the cumulant theorem

$$\left\langle e^{[\sum_{n\geq 0} j_n x_n]}\right\rangle = \exp\left[\left\langle e^{[\sum_{n\geq 0} j_n x_n]} - 1\right\rangle_c\right], \quad (28)$$

where $\langle\cdots\rangle_c$ denotes the connected part of the ensemble average. As shown in [10], it leads us to a partial resummation of the propagator as represented in Fig. (4) up to the one-loop order. Again, this is just a simplified version of Fig. (17) in [10] for the Lagrangian bias model. The grey ellipse represents all possible graphs attached with various number of wavy lines, i.e. Eq. (26). Compared to the diagram introduced in [10], we have omitted the summation sign over external wavy lines. Mathematically, such diagrammatical series is equivalent to

$$\begin{aligned}\Gamma_m^{(1)}(\mathbf{k}) &= \left\langle e^{-i\mathbf{k}\cdot\mathbf{\Psi}(0)}\int d^3\mathbf{p}\left[-i\mathbf{k}\cdot\frac{\delta}{\delta\phi(\mathbf{k}')}\mathbf{\Psi}(\mathbf{p})\right]\right\rangle \\ &= \Pi^{(0)}(\mathbf{k})\left\{\left\langle\frac{\delta}{\delta\phi(\mathbf{k}')}\exp\left[-i\mathbf{k}\cdot\mathbf{\Psi}(0)\right]\right\rangle_c\right\}\end{aligned} \quad (29)$$

Note that we have used an alternative version of the cumulant theorem in Eq. (28).

$$\left\langle e^{j_1x_1}x_2\right\rangle = \exp\left[\left\langle e^{j_1x_1}-1\right\rangle_c\right]\left\{\left\langle e^{j_1x_1}x_2\right\rangle_c\right\}. \quad (30)$$

which is obtained by taking the derivative of Eq. (28) respect to j_2 and then setting it to zero. We further calculate these contributions explicitly in the Appendix A. The result is not the same as the form originally proposed by [2]. However, the matching prescription between high-k and one-loop calculation in [2] seems more or less ad hoc. Therefore, an alternative way of constructing the propagators was proposed by [20], to which our calculation do agree. See [20] for the discussion of different versions of calculating multipoint propagators.

III. THE NON-LINEAR BIAS MODEL

A. Eulerian Bias Model

In Eulerian bias model, the galaxy number density perturbation at time η is considered as some general functional $F[\delta_m]$ of the underlying matter density distribution characterized by its Taylor coefficient b_n

$$\delta_E(\mathbf{x},\eta) = F\left[\delta_m(\mathbf{x},\eta)\right] = \sum_n\frac{b_n}{n!}\left[\delta_m(\mathbf{x},\eta)\right]^n, \quad (31)$$

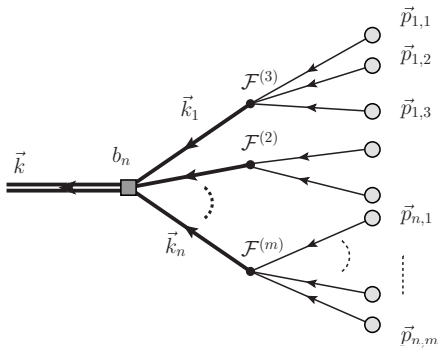

FIG. 5: Diagrammatic representation of $\delta_E(\mathbf{k},\eta)$ in Eulerian bias model.

where the nonlinear mass density field $\delta_m(\mathbf{x})$ is solved by perturbation theory mentioned in the last section. As discussed by [10], this functional is generally non-local. Therefore in Fourier space, bias coefficient b_n depends on wavenumbers

$$\begin{aligned}\delta_E(\mathbf{k},\eta) &= \sum_{n=1}^{\infty}\frac{1}{n!}\int d^3\mathbf{k}_{1\cdots n}\;\delta_D(\mathbf{k}-\mathbf{k}_{1\cdots n})b_n(\mathbf{k}_1,\cdots,\mathbf{k}_n) \\ &\quad\times\left[\delta_m(\mathbf{k}_1,\eta)\cdots\delta_m(\mathbf{k}_n,\eta)\right].\end{aligned} \quad (32)$$

In the local bias model, b_n then becomes constant times a smoothing window function $W(k,R)$ in Fourier space. In this model, the linear bias relation at large scale $P(k)\approx b^2P_m(k)$ is not only attributed to the first term in Eq. (32), but also from the higher orders b_n. As first pointed out by [17], the effective large scale bias is determined by infinite number of higher-point local variances of the field. Therefore, similar to the situation in the standard perturbation theory of matter density field, at later time when mass density variance grows larger, a naive perturbative expansion fails. In this case, such a breakdown affects both the large scale amplitude and the high-k regime of the power spectrum.

Given the definition of $\delta_E(\mathbf{k})$ in Eq.(32) and the diagrammatic representation of the density perturbation in Fig. (1), it is also possible to draw diagrams representing $\delta_E(\mathbf{k})$. As depicted in Fig.(5), each diagram contains two levels of nonlinear interactions. The thick solid n-branch tree represents the nonlinear convolution, and their interaction vertex, shown as a solid square, carries the bias coefficient $b_n/n!$, where n is the number of branches. Each branch represents one nonlinearly evolved density contrast $\delta_m(\mathbf{k}_n,\eta)$ at time η, which is followed by another m thin branches, to express its gravitational nonlinearity in terms of initial fields and perturbative kernels $\mathcal{F}^{(m)}$. At the end of each branch, small open circles represent the initial conditions δ_0. When expanding $\delta_E(\mathbf{k},\eta)$ to different orders, one should also include the information about the number of topologically equivalent diagrams, which essentially comes from the multinomial coefficient of $(\delta_m)^n$. The final field $\delta_E(\mathbf{k},\eta)$ is then a summation of

all possible diagrams.

B. Lagrangian Bias Model

To incorporate the halo bias with nonlinear perturbation theory, [12] proposed an alternative bias model involving the initial Lagrangian density fluctuation $\delta_0(\mathbf{q})$ instead of final Eulerian density $\delta_m(\mathbf{x},\eta)$. In this Lagrangian bias model, the non-linear objects, typically halos, were formed at some initial time with the number density is a functional $F[\delta_0(\mathbf{q})]$ of underlying linear density distribution δ_0. Then the Eulerian observable $\delta_L(\mathbf{x},\eta)$ at later time is described by the continuity relation

$$\begin{aligned} 1+\delta_L(\mathbf{x}) &= \int d^3\mathbf{q}\,[1+\delta_L(\mathbf{q})]\,\delta_D[\mathbf{x}-\mathbf{q}-\mathbf{\Psi}_L(\mathbf{q})] \\ &= \int d^3\mathbf{q}\; F[\delta_0(\mathbf{q})]\;\delta_D[\mathbf{x}-\mathbf{q}-\mathbf{\Psi}_L(\mathbf{q})], \end{aligned} \tag{33}$$

where $\mathbf{\Psi}_L(\mathbf{q})$ is the displacement field of such tracer. In Fourier space,

$$\delta_L(\mathbf{k},\eta) = \int d^3\mathbf{q}\; e^{-i\mathbf{k}\cdot\mathbf{q}}\left[F[\delta_0(\mathbf{q})]\; e^{-i\mathbf{k}\cdot\mathbf{\Psi}(\mathbf{q},\eta)}-1\right]. \tag{34}$$

In the limits that nonlinear objects trace exactly the underlying dark matter, i.e. $\mathbf{\Psi}_L = \mathbf{\Psi}_m$, one can further proceed to calculate the power spectrum $P(\mathbf{k})$ using Lagrangian perturbation theory of the matter field. In Fig. (6), we reproduced the diagram of this model introduced by [10] on the left, where the wavy line represents the displacement field $\mathbf{\Psi}_L$ and the n branches of thin solid lines with open circle symbolize the nth order of $F[\delta_0]$.

The great advantage of this approach is that it naturally takes account of the non-locality induced by gravitational evolution. As shown by [10], after perturbatively expanding both sides of Eq.(34) and comparing terms order by order, one obtains the relationship between Eulerian and Lagrangian bias parameters. To the first two orders [10],

$$\begin{aligned} b_1^E(\mathbf{k}) &= 1+b_1^L(\mathbf{k}), \\ b_2^E(\mathbf{k}_1,\mathbf{k}_2) &= b_2^L(\mathbf{k}_1,\mathbf{k}_2) - F_2(\mathbf{k}_1,\mathbf{k}_2)b_1^L(\mathbf{k}) + [\mathbf{k}\cdot L_1(\mathbf{k}_1)] \\ &\quad \times b_1^L(\mathbf{k}_2) + [\mathbf{k}\cdot L_1(\mathbf{k}_2)]\, b_1^L(\mathbf{k}_1). \end{aligned} \tag{35}$$

Therefore, even if the Lagrangian bias b_n^L is local initially, non-linear and non-local gravitational evolution $\mathcal{F}^{(n)}(\mathbf{p}_1,\cdots,\mathbf{p}_n)$ would render the Eulerian bias b_2^E nonlocal.

C. Continuous Galaxies Formation Model

As briefly mentioned in the introduction, we will try to generalize the Eulerian bias model in two different ways. As the resummation technique will be discussed in next two sections, in the following of this section, we will try to construct a model by combining Eulerian and Lagrangian pictures together.

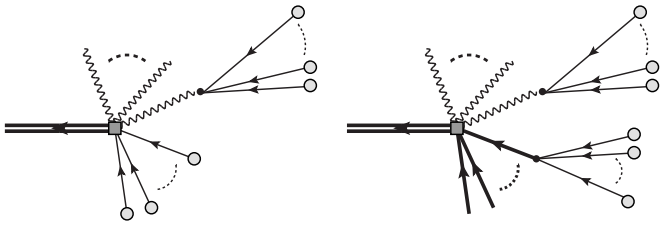

FIG. 6: Comparison between Lagrangian bias model (*left*) discussed in [4] and our galaxy formation model (*right*). The thin solid denotes the linear density perturbation δ_0, and thick line represents nonlinear overdensity $\delta_m(\eta)$. Note that the right diagram has not revealed very clearly the process of continuous galaxy formation as shown in Eq. (40).

First, we still assume that the complicated nonlinear process leading to the formation of galaxies or other type of observable tracers can be described by a general nonlinear functional $F[\delta_m(\eta)]$ at the moment of galaxy creation. In general this can be nonlocal, however, we will assume $F[\delta_m]$ to be local for simplicity. As what will be seen in the following, the locality assumption here is not as problematic as in the local Eulerian bias model since it only relates to the physical process during the moment of galaxy formation and could be easier to generalize. Furthermore, such functional can also explicitly depends on the formation time, i.e. we have $F[\delta_m(\eta),\eta]$ and $b_n(\mathbf{k}_{1\cdots,n},\eta)$.

Assuming at time η, there are $\Delta\rho_g(\mathbf{q},\eta)$ new galaxies were created during $\Delta\eta$ at a Lagrangian-like position $\mathbf{q}$, and then evolved to Eulerian position $\mathbf{x}$ where have been observed by a survey at time η_0. Analogous to the Lagrangian bias model (Eq. 33), this contributes to the Eulerian galaxies a number density $\rho_g(\mathbf{x},\eta_0)$

$$\int d^3\mathbf{q}\;\Delta\rho_g(\eta,\mathbf{q})\;\delta_D[\mathbf{x}-\mathbf{q}-\mathbf{\Psi}_g(\mathbf{q},\eta,\eta_0)], \tag{36}$$

where $\mathbf{\Psi}_g(\mathbf{q},\eta,\eta_0)$ is the displacement field of galaxy from η to η_0. Note that $\Delta\rho$ here only comprises galaxies that are finally selected in the sample. Therefore, the galaxy number density at observed time η_0 and comoving position $\mathbf{x}$ is a sum of all contributions that formed before η_0 and then moved to $\mathbf{x}$ with a displacement $\mathbf{\Psi}_g(\mathbf{q},\eta,\eta_0)$,

$$\begin{aligned} \rho_g(\mathbf{x},\eta_0) &= \int_{\eta_{min}}^{\eta_0} d\eta \int d^3\mathbf{q}\;\bar{\rho}_g'(\eta)F[\delta_m(\mathbf{q},\eta),\eta] \\ &\quad\times\;\delta_D[\mathbf{x}-\mathbf{q}-\mathbf{\Psi}_g(\mathbf{q},\eta,\eta_0)]. \end{aligned} \tag{37}$$

Here we have written the number density $\Delta\rho_g(\mathbf{q},\eta) = \overline{\Delta\rho}_g(\eta)F[\delta_m(\eta),\eta]$, where $\delta_m(\mathbf{q},\eta)$ is the nonlinear evolved matter density field at η. In principle, the displacement field of galaxies $\mathbf{\Psi}_g$ should follow the one of

dark matter $\mathbf{\Psi}_m$, i.e.

$$\mathbf{\Psi}_g(\mathbf{q};\eta,\eta_0) = b_\Psi\left[\mathbf{\Psi}_m(\mathbf{q}_{in},\eta_0) - \mathbf{\Psi}_m(\mathbf{q}_{in},\eta)\right], \quad (38)$$

where $\mathbf{q}_{in}$ is some initial Lagrangian position of the matter field when density perturbation is still linear. In the following of this paper, we will assume $b_\Psi = 1$. In the simplest case where all galaxies formed at η_f, i.e. $\bar{\rho}'_g(\eta) = \bar{\rho}_g\delta_D(\eta-\eta_f)$, a similar form of Eq.(33) is recovered. Taking the average of both sides of Eq.(37), one obtains the average number density $\bar{\rho}_g(\eta_0)$ as a integration of the average density over the whole galaxy formation history

$$\bar{\rho}_g(\eta_0) = \int_{\eta_{min}}^{\eta_0} d\eta\ \bar{\rho}'_g(\eta)\langle F[\delta_m,\eta]\rangle = \int_{\eta_{min}}^{\eta_0} d\eta\ \bar{\rho}'_g(\eta) \quad (39)$$

Therefore, the perturbation of galaxy number density can then be expressed as,

$$\begin{aligned}\delta_g(\mathbf{k},\eta_0) &= \int_{\eta_{min}}^{\eta_0} d\eta \int d^3\mathbf{q}\ f(\eta)\ e^{-i\mathbf{k}\cdot\mathbf{q}} F[\delta_m(\mathbf{q},\eta),\eta] \\ &\quad\times\ e^{-i\mathbf{k}\cdot\mathbf{\Psi}_g(\mathbf{q},\eta,\eta_0)} - \delta_D(\mathbf{k}). \end{aligned} \quad (40)$$

where $f(\eta) = \bar{\rho}'_g(\eta)/\bar{\rho}_g(\eta_0)$ denotes the average galaxies formation rate, with the normalization relation $\int d\eta\ f(\eta) = 1$. To first order, we have

$$\begin{aligned}\delta_g(\eta_0) &= \int_{\eta_{min}}^{\eta_0} d\eta\ f(\eta)\left[b_1 D(\eta) + b_\Psi\left[D(\eta_0) - D(\eta)\right]\right]\delta_0 \\ &= \left[b_\Psi D(\eta_0) + \int_{\eta_{min}}^{\eta_0} d\eta\ f(\eta) D(\eta)(b_1 - b_\Psi)\right]\delta_0, \end{aligned} \quad (41)$$

Therefore, the linear bias of galaxies evolves as

$$b_1^g(\eta_0) = b_\Psi + \int_{\eta_{min}}^{\eta_0} d\eta\ f(\eta)\frac{D(\eta)}{D(\eta_0)}[b_1 - b_\Psi]. \quad (42)$$

In the case that galaxies exactly trace cold dark matter, i.e. $b_\Psi = 1$, we recover the result calculated by [11] if only the growing mode is considered. As first discussed by [18], for the model galaxies burst at a single time η_f, $f(\eta) = \delta_D(\eta-\eta_f)$,

$$b_1^g(\eta_0) = 1 + \frac{D(\eta_f)}{D(\eta_0)}[b_1 - 1]. \quad (43)$$

So the gravitational growth will always debias the clustering of galaxies towards $b_1^g = 1$.

Because of this Lagrangian-like approach adopted here, this framework automatically incorporates the gravitational non-locality induced after the formation of the galaxies. Furthermore, as will be seen in Section V., Eq. (40) also allows the application of the resummation technique so that the perturbative convergence of such model is guaranteed.

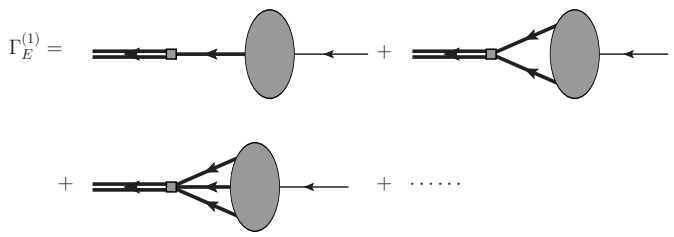

FIG. 7: Diagrammatical demonstration of the two-point nonlinear propagator $\Gamma_E^{(1)}(k)$ for Eulerian bias mode. The grey ellipse includes all possible ensemble averages among initial density perturbation δ_0.

IV. RESUMMED PERTURBATION THEORY OF EULERIAN BIAS MODEL

In this section, we will show that the Eulerian bias model can be partially resummed with the help of exponential decay of multipoint matter propagators $\Gamma_m^{(n)}$. Starting from the definition of this model (Eq. 32), one can define the $(n+1)$-point nonlinear propagator $\Gamma_E^{(n)}$ of the biased-tracer overdensity δ_E,

$$\begin{aligned}&\Gamma^{(n)}_{E,\ b_1\cdots b_n}(\mathbf{k}_1,\cdots,\mathbf{k}_n;\eta)\delta_D(\mathbf{k}-\mathbf{k}_{1\cdots n}) \\ &\qquad = \frac{1}{n!}\left\langle\frac{\delta^n\Xi_E(\mathbf{k})}{\delta\phi_{b_1}(\mathbf{k}_1)\cdots\delta\phi_{b_n}(\mathbf{k}_n)}\right\rangle. \end{aligned} \quad (44)$$

Before substituting δ_E (Eq. 32) as well as the perturbative solution of δ_m (Eq. 16, 18) into above definition, one first notices that, $\Gamma_E^{(n)}$ can be expanded in terms of the number of nonlinear density fields δ_m involved, just as depicted in the schematic diagram of Fig.(7) for the two-point propagator. Mathematically, it means $\Gamma_E^{(n)} = \sum_m \Gamma_E^{(n,\ m)}$, where

$$\begin{aligned}&\Gamma^{(n,\ m)}_{E,\ b_1\cdots b_n}(\mathbf{k}_1,\cdots,\mathbf{k}_n;\eta)\delta_D(\mathbf{k}-\mathbf{k}_{1\cdots n}) \\ &\quad = \frac{1}{n!m!}\int d^3\mathbf{q}_{1\cdots m}\ \delta_D(\mathbf{k}-\mathbf{q}_{1\cdots m}) b_m(\mathbf{q}_1,\cdots,\mathbf{q}_m) \\ &\qquad \left\langle\frac{\delta^n}{\delta\phi_{b_1}(\mathbf{k}_1)\cdots\delta\phi_{b_n}(\mathbf{k}_n)}\left[\Xi_m(\mathbf{q}_1)\cdots\Xi_m(\mathbf{q}_m)\right]\right\rangle. \end{aligned} \quad (45)$$

For the two-point propagator $\Gamma_E^{(1)}(\mathbf{k})$, let us write down all contributions formally. First of all, it is clear that the one-δ_m term, i.e. the first diagram in Fig.(7), equals the two-point propagator of the matter field itself $\Gamma_m^{(1)}(\mathbf{k})$ multiplied with the linear bias parameter $b_1(k)$. For the two-δ_m contribution, i.e. the second diagram, one reads from Eq. (45)

$$\begin{aligned}\Gamma^{(1,\ 2)}_{g,\ a}(\mathbf{k};\eta) &= 2\int d^3\mathbf{q}_{12}\ \delta_D(\mathbf{k}-\mathbf{q}_{12})\ \frac{b_2(\mathbf{q}_1,\mathbf{q}_2)}{2} \\ &\quad\times\ \left\langle\frac{\delta\Xi_m(\mathbf{q}_1,\eta)}{\delta\phi_a}\Xi_m(\mathbf{q}_2,\eta)\right\rangle \end{aligned} \quad (46)$$

As discussed in Section II, the ensemble average at the second line can be expanded by a $\Gamma-$like series, which in this case, is the propagator for matter field $\Gamma_m^{(n)}$. To proceed, we expand Eq. (46) explicitly

$$\begin{aligned}\Gamma^{(1,\ 2)}_{E,\ a}(\mathbf{k};\eta) \ =\ & \int d^3\mathbf{q}_{12}\ \delta_D(\mathbf{k}-\mathbf{q}_{12})\ b_2(\mathbf{q}_1,\mathbf{q}_2)\sum_{n_1,n_2}(n_1+1)\int d^3\mathbf{p}_{1\cdots n_1}d^3\mathbf{p}'_{1\cdots n_2}\ \delta_D(\mathbf{q}_1-\mathbf{k}-\mathbf{p}_{1\cdots n_1})\\ &\times\ \delta_D(\mathbf{q}_2-\mathbf{p}'_{1\cdots n_2})\ \mathcal{F}^{(n_1+1)}_{m,\ ac_1\cdots c_{n_1}}(\mathbf{k},\mathbf{p}_1,\cdots,\mathbf{p}_{n_1};\eta)\mathcal{F}^{(n_2)}_{m,\ d_1\cdots d_{n_2}}(\mathbf{p}'_1,\cdots,\mathbf{p}'_{n_2};\eta)\\ &\times\ \left\langle\phi_{c_1}(\mathbf{p}_1)\cdots\phi_{c_{n_1}}(\mathbf{p}_{n_1})\ \phi_{d_1}(\mathbf{p}'_1)\cdots\phi_{d_{n_2}}(\mathbf{p}'_{n_2})\right\rangle. \end{aligned}\tag{47}$$

As we have shown, Wick's theorem ensure the decomposition of joint ensemble average at the last line into the combinations of two-point correlations. Each of these terms can be labeled by three indices r_1, r_2, t, where $n_1 = 2r_1 + t$, $n_2 = 2r_2 + t$, i.e. we classify all pairs into three categories: r_1 pairs within the first field $\phi_{c_i}(\mathbf{p}_i)$, $(1 < i < n_1)$; r_2 pairs within the second field $\phi_{d_j}(\mathbf{p}'_j)$, $(1 < j < n_2)$; and t pairs in between. The renormalization is then achieved by realizing that a presummation of r_1 and r_2 gives rise to one $(t+2)$-point and another $(t+1)$-point propagator, therefore

$$\begin{aligned}\Gamma^{(1,\ 2)}_{E,\ a}(\mathbf{k};\eta) &= \sum_n (n+1)!\int d^3\mathbf{p}_{1\cdots n}\ P_0(p_1)\cdots P_0(p_n)\\ &\times\ b_2(\mathbf{k}+\mathbf{p}_{1\cdots n},-\mathbf{p}_{1\cdots n})\ \Gamma^{(n+1)}_{m,\ a}(\mathbf{k},\ \mathbf{p}_1,\cdots,\mathbf{p}_n;\eta)\\ &\times\ \Gamma^{(n)}_m(-\mathbf{p}_1,\cdots,-\mathbf{p}_n;\eta),\end{aligned}\tag{48}$$

where we have introduced the notation

$$\Gamma^{(n)}_m(\mathbf{p}_1,\cdots,\mathbf{p}_n;\eta) = \Gamma^{(n)}_{m,\ c_1\cdots c_n}(\mathbf{p}_1,\cdots,\mathbf{p}_n;\eta)\ u_{c_1}\cdots u_{c_n},\tag{49}$$

and used the definition of $\Gamma_m^{(n)}$ in terms of the perturbation kernel. The coefficient $n!$ then comes from all possible ways of matching n initial states with another group of n initial states. For this contribution, the only difference between Eq.(48) and Eq.(18) is the order of the matter propagator been summed. For the RPT description of the matter power spectrum, both propagators share the same order; otherwise, it would be impossible to match the pair. For the same reason, the order of one propagator in Eq.(48) is always greater than the other by one, since we have to select one branch out before taking the average.

The formula can be further generalized to arbitrary order n,

$$\begin{aligned}\Gamma^{(1,\ n)}_{E,\ a}(\mathbf{k};\eta) = \sum_{\{t_{ij}\}} g^{(1,\ n)}_{\{t_{ij}\}}\Bigg\{\int\Bigg[\prod_{1\le i<j\le n} d^3\mathbf{p}^{ij}_{1\cdots t_{ij}}\Bigg]\\ \times\ \frac{b_n(\mathbf{k},\mathbf{p}^{ij})}{n!}\ \Gamma^{(t_1+1)}_{m\ a}(\mathbf{k};\mathbf{p}^{11}_{1\cdots t_{11}},\cdots,\mathbf{p}^{1n}_{1\cdots t_{1n}};\eta)\\ \cdots\Gamma^{(t_n)}_m(\mathbf{p}^{n1}_{1\cdots t_{n1}},\cdots,\mathbf{p}^{nn}_{1\cdots t_{nn}};\eta)\prod_{1\le i<j\le n}\left[P_0(p^{ij})\right]^{t_{ij}}\Bigg\},\end{aligned}\tag{50}$$

where the index t_{ij} denotes the number of connections between the i-th and the j-th density field δ_m (e.g. $\{t_{ij}\} = \{t_{12}, t_{13}, t_{14}, t_{23}, t_{24}, t_{34}\}$ for $n = 4$), so the total number of the indices is then $n(n-1)/2$. The coefficient $g^{(1,\ n)}_{\{t_{ij}\}}$ is then given by

$$\begin{aligned}g^{(1,\ n)}_{\{t_{ij}\}} \ =\ & n\ (t_1+1)\ \Bigg[\prod_{1\le i\le n}\binom{t_i}{t_{i1}\cdots t_{in}}\Bigg]\\ &\times\Bigg[\prod_{1\le i<j\le n}(t_{ij})!\Bigg].\end{aligned}\tag{51}$$

Here, $t_i = \sum_m t_{im}$ is the total number of connections linked between the i-th density field δ_m and others, with $t_{ij} = t_{ji}$. Eq. (51) expresses the products of multinomial coefficients of choosing $\{t_{i1},\cdots,t_{in}\}$ from t_i for each density field, times all possible permutations within t_{ij} for pair matching. Each connection carries a momentum $\mathbf{p}^{ij}_l$, $(1 < l < t_{ij})$, which characterizes the l-th connection between i-th δ_m and j-th δ_m. The integration is taken over momenta of all possible connections among n different density fields. Because of the ensemble average Eq.(13), we have $\mathbf{p}^{ij}_{t_{ij}} = -\mathbf{p}^{ji}_{t_{ji}}$. $b_n(\mathbf{k},\mathbf{p}^{ij}) = b_n(\mathbf{k}+\sum_i\mathbf{p}^{1i},\sum_i\mathbf{p}^{2i},\cdots,\sum_i\mathbf{p}^{ni})$, and we also used the shorthand notation $[P_0(p^{ij})]^{t_{ij}}$ for $P_0(p^{ij}_1)\cdots P_0(p^{ij}_{t_{ij}})$.

Given above expressions, we are then able to expand $\Gamma_E^{(1)}$ in terms of the number of initial power spectra entering the calculation. For the tree level, it simply reads as

$$\Gamma^{(1,\ \mathrm{tree})}_{E,\ a}(\mathbf{k};\eta) = b_1(k)\ \Gamma^{(1)}_{m,\ a}(\mathbf{k};\eta;R)\tag{52}$$

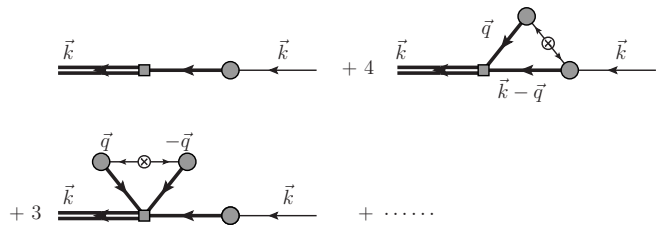

FIG. 8: Nonlinear propagator $\Gamma_E^{(1)}(k)$ of Eulerian bias model up to one-loop order. The integer in front of each diagram indicates the number of all topologically equivalent diagrams.

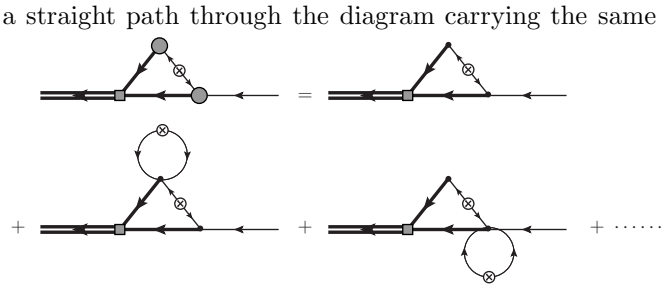

FIG. 9: Each diagram contains an infinite number of loop contributions.

where we have introduced the notation

$$\Gamma_m^{(n)}(\mathbf{p}_{1\cdots n};\eta;R)=\Gamma_m^{(n)}(\mathbf{p}_1\cdots\mathbf{p}_n;\eta)W(|\mathbf{p}_{1\cdots n}|R), \quad (53)$$

where $W(kR)$ is some smoothing window function.

At one-loop level, from Eq.(50), the contribution would be nonzero only when $n\leq 3$, since otherwise there would exist at least one Γ_m with zeroth order, which would vanish because $\Gamma_m^{(0)}=\langle\delta_m\rangle=0$. For $n=2$, $t_{12}=1$, the coefficient equals 4. For $n=3$, $t_{23}=1, t_{12}=t_{13}=0$, the coefficient equals 3. So we have

$$\begin{aligned}\Gamma_{E,\ a}^{(1,\ 1-\mathrm{loop})}(\mathbf{k};\eta)=&\int d^3\mathbf{q}\ P_0(q)\Big[\ \frac{b_3(\mathbf{k},\mathbf{q},-\mathbf{q})}{2}\\ \times&\ \big[\Gamma_m^{(1)}(\mathbf{q};\eta;R)\big]^2\Gamma_{m\ a}^{(1)}(\mathbf{k};\eta;R)+2\ b_2(\mathbf{k}-\mathbf{q},\mathbf{q})\\ &\times\ \Gamma_{m,\ a}^{(2)}(\mathbf{k},-\mathbf{q};\eta;R)\Gamma_m^{(1)}(\mathbf{q};\eta;R)\Big]. \end{aligned}\quad (54)$$

To make the Eq.(50) easier to understand, one can draw every contribution diagrammatically. Starting from the diagram representing $\delta_E^{(n)}$ in Fig.(5), we change all kernels into n-point propagators. After selecting one particular branch out, we glue the rest of the initial states (open circles) together. Every resultant topologically inequivalent diagram represents one or several terms in Eq.(50). Since all ordinary kernels have already been substituted by propagators, the ensemble average (gluing) is only performed among different density fields δ_m. In Fig.(8), we show all diagrams of $\Gamma_E^{(1)}$ up to one-loop order. They correspond one-to-one to Eq.(52) and Eq.(54). We also present all two-loop diagrams and equations of $\Gamma_E^{(1)}$ in Appendix B. It should be emphasized that, by substituting ordinary kernels into propagators, each diagram in fact contains an infinite number of loop contributions at every substituting position, as shown in Fig.(9).

Numerically, the Gaussian damping of the multipoint matter propagator $\Gamma_m^{(n)}$ will eventually contribute to the improvement of the convergence in calculating nonlinear matter power spectrum. Therefore, it is important to check whether $\Gamma_E^{(n)}$ share the similar feature. From diagrams representing $\Gamma_E^{(1)}(k)$, we see that there exists a straight path through the diagram carrying the same momentum $\mathbf{k}$ at both the start and end. Along this path, there is one convolution bias vertex b_n, as well as one $(n+1)$-point propagator $\Gamma_m^{(n)}$. For $n=1$ (e.g. the third diagram in Fig.(8)), this contribution recovers the same k-dependence as $\Gamma_m^{(1)}(k)$, rescaled by a constant from loop integration. When $n>1$, Eq.(17) suggests a similar damping of $\mathbf{k}$ given $\mathbf{p}_1\cdots\mathbf{p}_{n-1}$. Meanwhile every propagator associates with a smoothing window function $W(kR)$. Therefore one should expect that, in the large-k limit, $\Gamma_E^{(1)}$ will decay as a combined effect of a Gaussian damping of $\Gamma_m^{(1)}$ and the smoothing window function.

Besides the tree level result of two-point propagator $\Gamma_E^{(1,\ \mathrm{tree})}(k)$, which equals the one of dark matter field times the linear bias coefficient $b_1(k)\Gamma_m^{(1)}(k)$, the loop integration from higher-order calculation, e.g. the third diagram in Fig.(8), will also change the small-k normalization of $\Gamma_E^{(1)}(k)$ and eventually the effective large-scale bias of the power spectrum b_1^*. As we will see at the end of this section, $\Gamma_E^{(1)}(k)$ dominates the contribution of b_1^*, hence the accuracy of the b_1^* depends on the precision of estimating the $\Gamma_E^{(1)}(k)$. Due to the exponential decay of matter propagators $\Gamma_m^{(n)}$, our resummed formula will help us in improving the convergence of b_1^*.

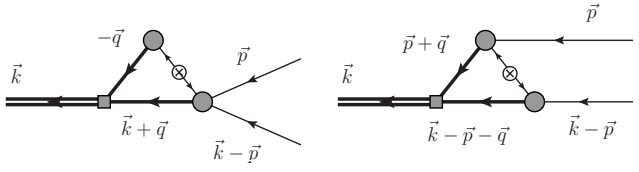

FIG. 10: Examples of two different contributions of three-point propagator, full set of diagrams is shown in the Appendix B.

Now, we can further derive the three-point propagator similarly, except that two distinct contributions have to be taken into account because of the second order functional derivative in the definition of $\Gamma_E^{(2)}$.

$$\Gamma^{(2,\ n)}_{E,\ ab}(\mathbf{k}_1,\mathbf{k}_2;\eta) \ = \ \frac{n}{2}\ \int d^3\mathbf{q}_{1\cdots n}\ \delta_D(\mathbf{k}-\mathbf{q}_{1\cdots n})\ \frac{b_n(\mathbf{q}_1,\cdots,\mathbf{q}_n)}{n!}\left[\left\langle\frac{\delta^2\Xi_m(\mathbf{q}_1,\eta)}{\delta\phi_a\delta\phi_b}\Xi_m(\mathbf{q}_2,\eta)\cdots\Xi_m(\mathbf{q}_n,\eta)\right\rangle\right.$$
$$\left.+\ (n-1)\ \left\langle\frac{\delta\Xi_m(\mathbf{q}_1,\eta)}{\delta\phi_a}\frac{\delta\Xi_m(\mathbf{q}_2,\eta)}{\delta\phi_b}\Xi_m(\mathbf{q}_3,\eta)\cdots\Xi_m(\mathbf{q}_n,\eta)\right\rangle\right] \tag{55}$$

As shown in Eq.(55), the first term takes the joint average of the products of a second derivative with $n-1$ density fields. Diagrammatically speaking, it corresponds to selecting two branches from a single δ_m, i.e. the first diagram in Fig. (10). In Fig. (18) of Appendix C, this category includes the first, third and sixth diagram. The rest of the diagrams then correspond to the second term of Eq.(55), where two branches originate from two different density fields. Both terms can be written in the same form of Eq.(50),

$$\Gamma^{(2,\ n)}_{E,\ ab}(\mathbf{k}_1,\mathbf{k}_2;\eta) \ = \ \sum_{\{t_{ij}\}}\ \int\ \left[\prod_{1\le i<j\le n} d^3\mathbf{p}^{ij}_{1\cdots t_{ij}}\right]\frac{b_n(\mathbf{k},\mathbf{p}^{ij})}{n!}\ \left[g^{(2,\ n)}_{\{t_{ij}\}}\ \Gamma^{(t_1+2)}_{m,\ ab}(\mathbf{k}_1,\mathbf{k}_2;\mathbf{p}^{11}_{1\cdots t_{11}},\cdots,\mathbf{p}^{1n}_{1\cdots t_{1n}})\right.$$
$$\times\cdots\times\ \Gamma^{(t_n)}_m(\mathbf{p}^{n1}_{1\cdots t_{n1}},\cdots,\mathbf{p}^{nn}_{1\cdots t_{nn}})\ +\ \tilde{g}^{(2,\ n)}_{\{t_{ij}\}}\ \Gamma^{(t_1+1)}_{m,\ a}(\mathbf{k}_1;\mathbf{p}^{11}_{1\cdots t_{11}},\cdots,\mathbf{p}^{1n}_{1\cdots t_{1n}})$$
$$\left.\times\ \Gamma^{(t_2+1)}_{m,\ b}(\mathbf{k}_2;\mathbf{p}^{21}_{1\cdots t_{21}},\cdots,\mathbf{p}^{2n}_{1\cdots t_{2n}})\cdots\Gamma^{(t_n)}_m(\mathbf{p}^{n1}_{1\cdots t_{n1}},\cdots,\mathbf{p}^{nn}_{1\cdots t_{nn}})\right]\prod_{1\le i<j\le n}\left[P_0(p^{ij})\right]^{t_{ij}} \tag{56}$$

The difference between the two terms can be clearly seen from their orders of the matter propagators. With the same labeling system, the first gives $\Gamma^{(t_1+2)}_m\Gamma^{(t_2)}_m\cdots\Gamma^{(t_n)}_m$, while the second gives $\Gamma^{(t_1+1)}_m\Gamma^{(t_2+1)}_m\cdots\Gamma^{(t_n)}_m$. Meanwhile, the two g coefficients equal

$$g^{(2,\ n)}_{\{t_{ij}\}} \ = \ \frac{n}{2}(t_1+2)(t_1+1)\left[\prod_{1\le i\le n}\binom{t_i}{t_{i1}\cdots t_{in}}\right]$$
$$\times\left[\prod_{1\le i<j\le n}(t_{ij})!\right],$$
$$\tilde{g}^{(2,\ n)}_{\{t_{ij}\}} \ = \ \frac{n(n-1)}{2}(t_1+1)(t_2+1)\left[\prod_{1\le i\le n}\binom{t_i}{t_{i1}\cdots t_{in}}\right]$$
$$\times\left[\prod_{1\le i<j\le n}(t_{ij})!\right]. \tag{57}$$

The first contribution $g^{(2,\ n)}_{\{t_{ij}\}}$ gives $n(t_1+2)(t_1+1)$, while the second term $\tilde{g}^{(2,\ n)}_{\{t_{ij}\}}$ gives $n(n-1)(t_1+1)(t_2+1)$.

At tree level, there are two diagrams: one is $b_1(k)\Gamma^{(2)}_m$, from the single-δ_m contribution; and the other is the two-δ_m term with $t_{12}=0$ for the second term of Eq.(56),

$$\Gamma^{(2,\ \mathrm{tree})}_{E,\ ab}(\mathbf{p},\mathbf{k}-\mathbf{p};\eta;R) = b_1(\mathbf{k})\ \Gamma^{(2)}_{m,\ ab}(\mathbf{p},\mathbf{k}-\mathbf{p};\eta;R)$$
$$+\ \frac{b_2(\mathbf{k}-\mathbf{p},\mathbf{p})}{2}\ \Gamma^{(1)}_{m,\ a}(\mathbf{p};\eta;R)\Gamma^{(1)}_{m,\ b}(\mathbf{k}-\mathbf{p};\eta;R). \tag{58}$$

All the one-loop contributions can be found in the Appendix C.

Finally, the non-linear power spectrum of the field δ_E can be expressed as

$$P_E(k;\eta) \ = \ \sum_{n\ge1} n!\int d^3\mathbf{q}_{1\cdots n}\ \delta_D(\mathbf{k}-\mathbf{q}_{1\cdots n})P_0(q_1)\cdots P_0(q_n)$$
$$\times\ \left[\Gamma^{(n)}_E(\mathbf{q}_1,\cdots,\mathbf{q}_n;\eta)\right]^2 \tag{59}$$

In Fig. (11), we illustrate the numerical calculation of the power spectrum of Eulerian bias model at redshift $z=0.5$ for bias parameters $b_1=1.5$, $b_2=0.5$ and $b_3=0.2$, assuming a spherical top-hat smoothing length $R=2\mathrm{Mpc}/h$. The solid line gives the full nonlinear power spectrum of $P_E(k)$ including both $\Gamma^{(1)}_E$ and $\Gamma^{(2)}_E$ contributions. Each of them is then represented by the long dashed and the short dashed line respectively. We only calculate the $\Gamma^{(2)}_E$ up to one-loop order while $\Gamma^{(1)}_E$ to the two-loop order. Compared to the dot-dashed line representing the linear bias contribution $b_1^2P_L(k)$, one sees

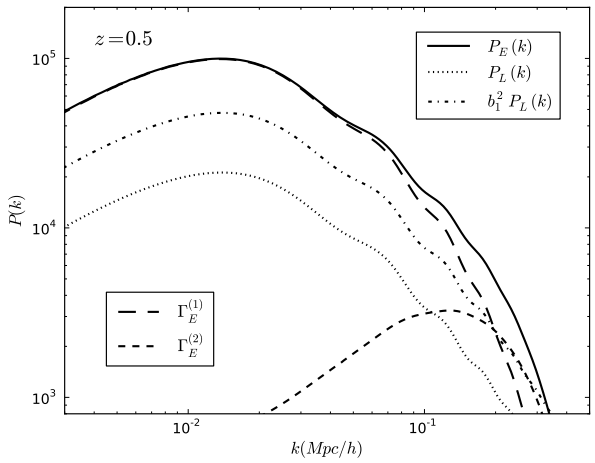

FIG. 11: The power spectrum of Eulerian bias model at $z = 0.5$ with $b_1 = 1.5,\ b_2 = 0.5$ and $b_3 = 0.2$, assuming a spherical top-hat smoothing window function with $R = 2Mpc/h$. The solid line gives the full result $P_E(k)$ including both $\Gamma_E^{(1)}$ and $\Gamma_E^{(2)}$ contributions, while each of them are represented in long dashed as well as short dashed line respectively. Here, $\Gamma_E^{(1)}$ is calculated up to two-loop order and $\Gamma_E^{(2)}$ to the one-loop order. The dotted line shows the linear matter power spectrum $P_L(k)$, and the dot-dashed line illustrates the linear bias contribution $b_1^2 P_L(k)$. The offset between the dot-dashed and solid curve indicates that higher order bias parameters contribute to the large-scale amplitude of the power spectrum.

clearly that higher order bias parameters contribute to the large-scale amplitude of the power spectrum. This can also be seen in the left panel of Fig. (14), where we plot the normalized two-point propagator $\Gamma_E^{(1)}(k,z)/D(z)$ for the same bias model but at various redshifts, starting from $z = 6$ to $z = 0.5$. At lower redshift, the variance of the local density field grows larger, so does the effective linear bias b_1^* as shown in the figure. For the same reason, the exponential damping length decrease towards higher redshift. As expected, all of lines at large scale lie above the true linear bias b_1, i.e. the dotted horizontal line. We want to remind here that the accuracy of such effective large scale bias calculated by our formalism has already been verified with the simulation in [16] for a logarithmic transformation. It is guaranteed by incorporating the matter propagator, since the loop integrations, that contribute to b_1^*, are reduced and therefore the series expansion is regulated.

Another distinguishing feature provided by our formula is the scale-dependent bias. In Fig.(12), we give several examples of such scale-dependent deviation at baryonic acoustic oscillation sclaes compared to the linear matter power spectrum at two different redshifts for various bias parameters. They are calculated by dividing out the no-wiggle power spectrum [19] with appropriate normalizations. As can be seen in the figure, such scale dependence is, roughly speaking, determined by the relative value of linear bias b_1 and high-order b_n. So for a fixed linear bias, a bigger high-order b_n leads to a larger scale-dependent deviation, while a smaller b_1 results in the similar trend if b_n are fixed. Not surprisingly, the same bias model will give a larger deviation at lower redshift.

V. RESUMMED PERTURBATION THEORY OF CONTINUOUS GALAXY FORMATION MODEL

Based on the construction of resummed perturbation theory of Eulerian bias model in the last section, we will further extend such model to incorporate a continuous galaxies formation history. As shown in Eq.(40), the perturbation of galaxy number density observed at η_0 can be expressed as,

$$\delta_g(\mathbf{k},\eta_0) \ = \ \Xi_g(\mathbf{k},\eta_0) = \int_{\eta_{min}}^{\eta_0} d\eta\ f(\eta)\Delta_g(\mathbf{k},\eta,\eta_0). \tag{60}$$

where the integrand $\Delta_g(\mathbf{k};\eta,\eta_0)$ is the density contrast of galaxies formed at η and then been observed at η_0

$$\begin{aligned}
\Delta_g(\mathbf{k}) \ &= \ \int d^3\mathbf{q}\ e^{-i\mathbf{k}\cdot\mathbf{q}}\left[F[\delta_m(\mathbf{q},\eta),\eta]e^{-i\mathbf{k}\cdot\mathbf{\Psi}_g(\mathbf{q},\eta,\eta_0)}-1\right] \\
&= \ \left[\widetilde{F} * \widetilde{e^{-i\mathbf{k}\cdot\mathbf{\Psi}_g}}\right](\mathbf{k},\eta,\eta_0) - \delta_D(\mathbf{k}) \\
&= \ \sum_{n+m\geq 1}^{\infty}\frac{(-i)^m}{n!\ m!}\int d^3\mathbf{k}_{1\cdots n}d^3\mathbf{k}'_{1\cdots m} \\
&\quad \times\ \delta_D(\mathbf{k}-\mathbf{k}_{1\cdots n}-\mathbf{k}'_{1\cdots m})b_n(\mathbf{k}_1,\cdots,\mathbf{k}_n;\eta) \\
&\quad \times\ [\delta_m(\mathbf{k}_1,\eta)\cdots\delta_m(\mathbf{k}_n,\eta)]\ \ [\mathbf{k}\cdot\mathbf{\Psi}_g(\mathbf{k}'_1,\eta,\eta_0)] \\
&\quad \times\ \cdots\ \ [\mathbf{k}\cdot\mathbf{\Psi}_g(\mathbf{k}'_m,\eta,\eta_0)]
\end{aligned} \tag{61}$$

where $\widetilde{F}$ and $\widetilde{e^{-i\mathbf{k}\cdot\mathbf{\Psi}_g}}$ are Fourier transforms of F and $e^{-i\mathbf{k}\cdot\mathbf{\Psi}_g}$ respectively, and $*$ denotes the convolution. Apart from the weighted average of Δ_g with the galaxy formation rate $f(\eta)$, this model differs from the work of [12] in two ways. First, the non-linear bias functional $F[\delta_m]$ depends on the nonlinear evolved matter field $\delta_m(\eta)$ instead of initial state δ_0. Secondly, the displacement field $\mathbf{\Psi}_g(\eta,\eta_0)$ characterizes the movement of the galaxy from location $\mathbf{q}$ at time η to Eulerian position $\mathbf{x}$ of time η_0. In the following, we will construct the propagator of $\delta_g(\mathbf{k},\eta_0)$ instead of following the work of [12] exactly.

Starting from Eq.(60), one can define the multi-point propagator of galaxies similarly. For the two-point propagator $\Gamma_g^{(1)}(k)$, we have

$$\begin{aligned}
\left\langle\frac{\delta\Xi_g(\mathbf{k},\eta_0)}{\delta\phi(\mathbf{k}')}\right\rangle \ &= \ \Gamma_g^{(1)}(\mathbf{k},\eta_0)\delta_D(\mathbf{k}-\mathbf{k}') \\
&= \ \int_{\eta_{min}}^{\eta_0} d\eta\ f(\eta)\ \left\langle\frac{\delta\Delta_g(\mathbf{k},\eta,\eta_0)}{\delta\phi(\mathbf{k}')}\right\rangle
\end{aligned} \tag{62}$$

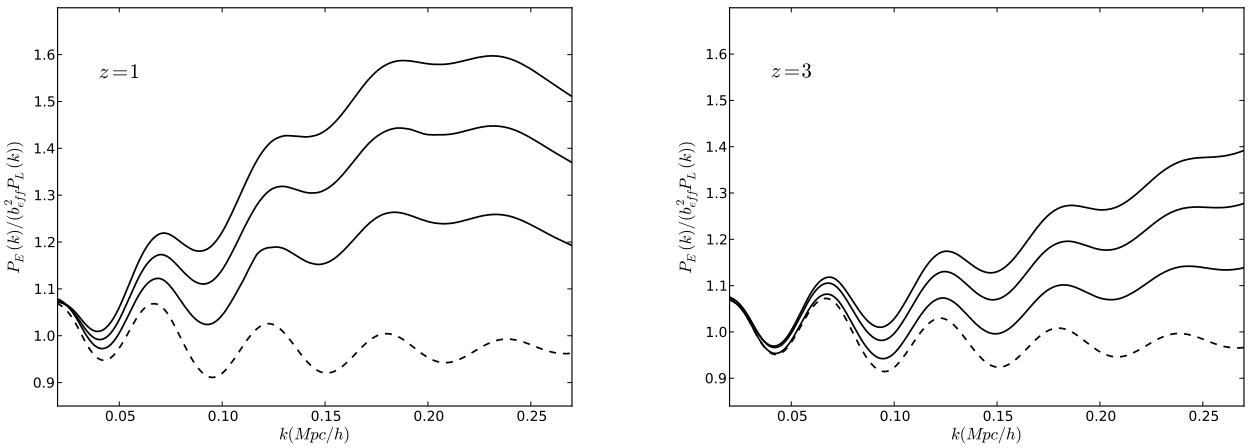

FIG. 12: Examples of scale-dependent deviation of nonlinear Eulerian bias model at scales of baryonic acoustic oscillation for various bias parameters at redshift $z = 1$ (*left*) and $z = 3$ (*right*). Both $\Gamma_E^{(1)}$ and $\Gamma_E^{(2)}$ are calculated up to the one-loop order. From the top to bottom, we adopt bias parameters: (1) $b_1 = 0.8,\ b_2 = 1.5,\ b_3 = 0.4$; (2) $b_1 = 0.8,\ b_2 = 1,\ b_3 = 0.2$; (3) $b_1 = 1,\ b_2 = 0.5,\ b_3 = 0.2$.

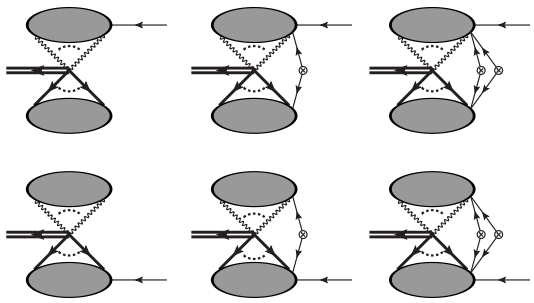

FIG. 13: Diagrams of $\Gamma_g^{(1)}(\mathbf{k})$ up to the two-loop order. The first row represents the contribution of $\Gamma^{(1)}_{g,\ 2}(k)$ and the second row for $\Gamma^{(1)}_{g,\ 1}(k)$ terms.

Concentrating on the quantity inside the integration, and we define

$$\left\langle \frac{\delta\Delta_g(\mathbf{k};\eta,\eta_0)}{\delta\phi(\mathbf{k}')} \right\rangle \ = \ \Gamma_g^{(1)}(\mathbf{k};\eta,\eta_0)\delta_D(\mathbf{k}-\mathbf{k}') \quad (63)$$

Substituting the expression of Eq.(61) into this definition, one immediately obtains two different contributions arising from the functional derivative

$$\begin{aligned}\Gamma_g^{(1)}(\mathbf{k};\eta,\eta_0) &= \Gamma^{(1)}_{g,\ 1}(\mathbf{k};\eta,\eta_0) + \Gamma^{(1)}_{g,\ 2}(\mathbf{k};\eta,\eta_0) \\ &= \left\langle \left[\frac{\delta}{\delta\phi(\mathbf{k})}\widetilde{F}\right] * \widetilde{e^{-i\mathbf{k}\cdot\mathbf{\Psi}_g}} \right\rangle + \left\langle \widetilde{F} * \left[\frac{\delta}{\delta\phi(\mathbf{k})}\widetilde{e^{-i\mathbf{k}\cdot\mathbf{\Psi}_g}}\right] \right\rangle\end{aligned} \quad (64)$$

Concentrating on $\Gamma^{(1)}_{g,\ 1}(\mathbf{k};\eta,\eta_0)$ first, a further perturbative expansion gives

$$\begin{aligned}\Gamma^{(1)}_{g,\ 1} = \Big\langle \sum_{n=1}^{\infty} \int d\mathbf{k}_{1\cdots n} \frac{b_n(\mathbf{k},\mathbf{k}_1,\cdots\mathbf{k}_n)}{n!} \Big[\delta_m(\mathbf{k}_1)\cdots\delta_m(\mathbf{k}_n) \\ \times \frac{\delta}{\delta\phi}\delta_m(\mathbf{k})\Big] \times \sum_{m=0}^{\infty}\frac{(-i)^m}{m!}\int d\mathbf{k}'_{1\cdots m}\,[\mathbf{k}\cdot\mathbf{\Psi}_g(\mathbf{k}'_1)]\cdots \\ \times\ \cdots\ [\mathbf{k}\cdot\mathbf{\Psi}_g(\mathbf{k}'_m)]\Big\rangle\end{aligned} \quad (65)$$

Without going into detail, one finds the resemblance between above equation and Eq. (46, 47), since both $\widetilde{F}$ and $\widetilde{e^{-i\mathbf{k}\cdot\mathbf{\Psi}_g}}$ can be written in the form of Eq. (19). Therefore, following the exact same procedure after Eq. (46), the contribution $\Gamma^{(1)}_{g,\ 1}$ can be similarly resummed using the $\Gamma-$expansion, and one simply reads from Eq. (48) as

$$\begin{aligned}\Gamma^{(1)}_{g\ ,1}(\mathbf{k};\eta,\eta_0) = \sum_n (n+1)!\int d^3\mathbf{p}_{1\cdots n}\ \Big[P_0(\mathbf{p}_{1\cdots n})\Big]^n \\ \times\ \Gamma_E^{(n+1)}(\mathbf{k},\mathbf{p}_1,\cdots,\mathbf{p}_n;\eta)\Pi_k^{(n)}(\mathbf{p}_1,\cdots,\mathbf{p}_n;\eta,\eta_0)\end{aligned} \quad (66)$$

Here the first contribution, arisen from $\langle\delta\tilde{F}/\delta\phi(\mathbf{k})\rangle$, is the multipoint propagator of Eulerian biased tracer $\Gamma_E^{(n)}$ which we have discussed in the last section, and the second contribution is defined as

$$\Pi_k^{(n)}(\mathbf{p}_1,\cdots,\mathbf{p}_n;\eta,\eta_0) = \frac{1}{n!}\left\langle \frac{\delta^n\ \widetilde{e^{-i\mathbf{k}\cdot\mathbf{\Psi}_g}}(\mathbf{p};\eta,\eta_0)}{\delta\phi(\mathbf{p}_1)\cdots\delta\phi(\mathbf{p}_n)} \right\rangle \quad (67)$$

where $\mathbf{p} = \mathbf{p}_{1\cdots n}$. When $\mathbf{k} = \mathbf{p}$, it recovers to the definition of multipoint matter propagators in Lagrangian perturbation theory with galaxy displacement field $\mathbf{\Psi}_g(\eta,\eta_0)$.

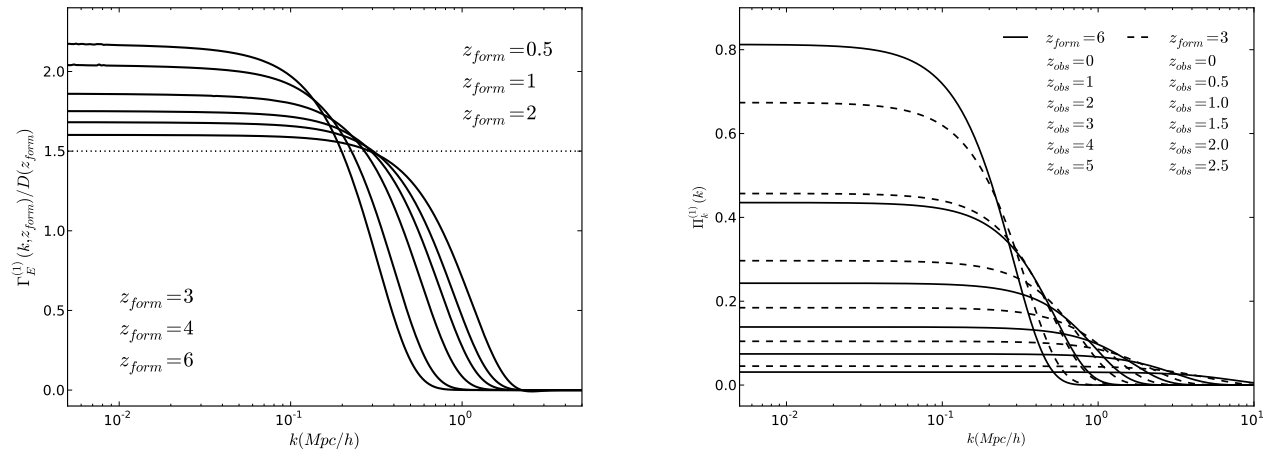

FIG. 14: (*left*): Two-point propagator of Eulerian bias model $\Gamma_E^{(1)}(k)$ at various redshifts $z_{form} = 0.5,\ 1,\ 2,\ 3,\ 4$ and 6 from top to bottom. We assume the bias parameters $b_1 = 1.5,\ b_2 = 0.5,\ b_3 = 0.2$ and 0 otherwise. (*right*): $\Pi_k^{(1)}(\mathbf{k}; z_{form}, z_{obs})$ (Eq. 67), from $z_{form} = 3$ and 6 evolved to $z_{obs} = 0,\ 0.5,\ 1,\ 1.5,\ 2$ and 2.5 (*top to bottom*).

The physical consequence of Eq. (66) is the separation between the nonlinear gravitational evolution of galaxies after their creation characterized by $\Pi_k^{(n)}$ and the more complicated nonlinear galaxy formation physics parameterized by the unknown functional $F[\delta_m]$. The final nonlinear growth of galaxy density perturbation $\Gamma_g^{(1)}$ relates to these two physical processes in a statistical way. Diagrammatically, Starting from the second diagram in Fig. (6), one can construct $\Gamma_E^{(n)}$ and $\Pi_k^{(n)}$ simply by gluing initial states connected to wavy line and thick solid line separately. We illustrate $\Gamma_{g,\,1}^{(1)}(k)$ in the second row of Fig. (13) up to the two-loop order.

Similarly, the second term in Eq. (64)

$$\Gamma_{g,2}^{(1)} = \left\langle \sum_{n=1}^{\infty} \int d\mathbf{k}_{1\cdots n} \frac{b_n(\mathbf{k}_1,\cdots \mathbf{k}_n;\eta)}{n!} \delta_m(\mathbf{k}_1)\cdots\delta_m(\mathbf{k}_n) \times \sum_{m=0}^{\infty} \frac{(-i)^m}{m!} \int d\mathbf{k}'_{1\cdots m} \left[\mathbf{k}\cdot\mathbf{\Psi}_g(\mathbf{k}'_1)\right]\cdots\left[\mathbf{k}\cdot\mathbf{\Psi}_g(\mathbf{k}'_m)\right] \times \left[\mathbf{k}\cdot\frac{\delta\mathbf{\Psi}_g(\mathbf{k}'_{m+1})}{\delta\phi(\mathbf{k}')}\right]\right\rangle \quad (68)$$

can be resummed as

$$\Gamma_{g\ ,2}^{(1)}(\mathbf{k};\eta,\eta_0) = \sum_n (n+1)! \int d^3\mathbf{p}_{1\cdots n} \left[P_0(\mathbf{p}_{1\cdots n})\right]^n \times \Gamma_E^{(n)}(\mathbf{k},\mathbf{p}_1,\cdots,\mathbf{p}_n;\eta)\Pi_k^{(n+1)}(\mathbf{k},\mathbf{p}_1,\cdots,\mathbf{p}_n;\eta,\eta_0), \quad (69)$$

which corresponds to the first row of Fig.(13). Therefore, up to the one-loop order, the two-point propagator of galaxy density perturbation $\Gamma_g^{(1)}(k)$ equals

$$\Gamma_g^{(1)}(\mathbf{k};\eta,\eta_0) \approx \Gamma_E^{(1)}(\mathbf{k};\eta) + \Pi_k^{(1)}(\mathbf{k};\eta,\eta_0) + 2\int d^3\mathbf{p}\ P_0(p) \left[\Gamma_E^{(2)}(\mathbf{k},\mathbf{p};\eta)\Pi_k^{(1)}(\mathbf{p};\eta,\eta_0) + \Gamma_E^{(1)}(\mathbf{p};\eta)\Pi_k^{(2)}(\mathbf{k},\mathbf{p};\eta,\eta_0)\right] \quad (70)$$

To proceed, we have to estimate the $\Pi_k^{(n)}$ with galaxy displacement field $\mathbf{\Psi}_g(\eta,\eta_0)$. To the first order, the Zel'dovich approximation simply gives

$$\mathbf{\Psi}_g^{(1)}(\mathbf{k};\eta,\eta_0) = [D(\eta_0) - D(\eta)]\delta_0(\mathbf{k}), \quad (71)$$

and therefore,

$$\Pi_k^{(1)}(k;\eta,\eta_0) \approx [D_0 - D]\exp\left[-\frac{k^2(D_0-D)^2}{2}\sigma_\Psi^2\right], \quad (72)$$

where $D_0 = D(\eta_0)$, and $D = D(\eta)$. So it is fully characterized by the gravitational growth between two different moments. Though higher order corrections analogous to the calculation in Appendix A are possible, we haven't explicitly calculated them here. The caveat is that the galaxy displacement field at $\mathbf{q}$ relates to $\mathbf{\Psi}_m$ at some initial Lagrangian position $\mathbf{q}_{in}$ since we assume

$$\mathbf{\Psi}_g(\mathbf{q};\eta,\eta_0) = \mathbf{\Psi}_m(\mathbf{q}_{in};\eta_0) - \mathbf{\Psi}_m(\mathbf{q}_{in};\eta). \quad (73)$$

At the lowest order $\mathbf{q} = \mathbf{q}_{in}$, but the coordinate transform needs to be carefully incorporated for higher order calculation. Furthermore, a more reliable approach is to directly solve the fundamental dynamical equation (Eq. 8) with the potential determined by the nonlinear matter distribution at η. We will leave this in the future work

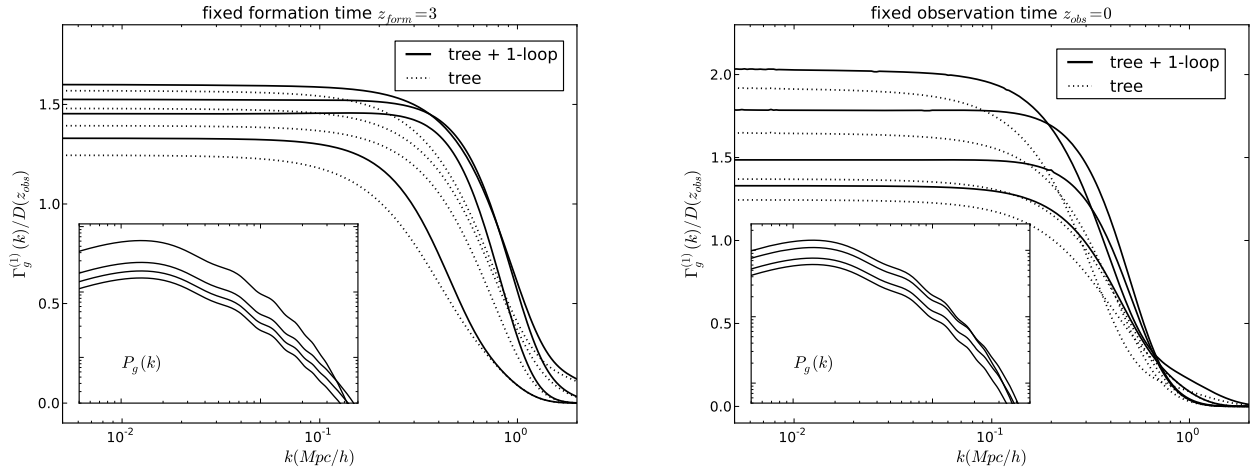

FIG. 15: The normalized two-point propagator $\Gamma_g^{(1)}(k;\ z_{form},\ z_{obs})/D(z_{obs})$ of galaxies which formed at fixed formation redshift (*left*) $z_{form}=3$, and observed at $z_{obs}=2,\ 1.5,\ 1$ and 0 (*top to bottom*); and at fixed observation redshift (*right*) $z_{obs}=0$, and formed at $z_{form}=0.5,\ 1,\ 2$ and 3 (*top to bottom*). Assuming nonlinear bias model $b_1=1.5,\ b_2=0.5,\ b_3=0.2$. *Inner panel:* the corresponding power spectra in the opposite/same (*left*/*right*) order.

and simply utilize the Zel'dovich approximation (Eq. 72) within this paper.

In the right panel of Fig. (14), we illustrate the $\Pi_k^{(1)}(k)$ from the moment of galaxy formation $z_{form}=3$ and 6 evolve to various observational time z_{obs}. At the large scale, it converges to linear result $D(z_{obs})-D(z_{form})$, which relates to the linear debiasing we discussed in Eq. (42), and dampens to zero towards smaller scales with the speed proportional to $[D(z_{obs})-D(z_{form})]^2$. As can be seen in the figure, when galaxies have more time to evolve , i.e. $z_{obs}-z_{form}$ is large, the observed galaxy distribution is more influenced by gravitational evolution. This can be easily seen from Eq. (70), since at tree level $\Gamma_g^{(1)}(k)=\Gamma_E^{(1)}(k;z_{form})+\Pi_k^{(1)}(k;z_{form},z_{obs})$. When $D(z_{obs})-D(z_{form})$ is small, $\Pi_k^{(1)}(k;z_{form},z_{obs})$ vanish and therefore the gravitational evolution is negligible.

This can also be clearly seen in the left panel of Fig. (15), where we plot the normalized galaxy propagator $\Gamma_g^{(1)}(k;z_{form},z_{obs})/D(z_{obs})$ with fixed formation redshift $z_{form}=3$ and observed at various z_{obs}. The dashed line shows the tree level of Eq. (70) and solid line corresponds to 1-loop results. In this situation, $\Gamma_E^{(n)}$ is fixed, and as z_{obs} decreases from 2 to 0, the large scale bias also decreases as expected. However, the amplitude of the power spectrum itself as shown in the inner panel of left Fig. (15), is still increasing at lower redshift due to the linear growth $D(z_{obs})$. From the diagrams of three-point propagator of Eulerian bias model, at large scale $k\to 0$, $\Gamma_E^{(2)}(\mathbf{k},\mathbf{p})$ is nonzero, hence the loop integration also contributes to the large scale bias, although it's still dominated by the tree-level value. As for smaller scales, $\Gamma_g^{(1)}$ dampens qualitatively similar to the $\Pi_k^{(1)}(k)$.

In the right panel of Fig. (15), we illustrate the same quantity for fixed observation redshift $z_{obs}=0$, when galaxies are formed at different time with the same nonlinear process (same $F[\delta_m]$ and b_n). In this case, both $\Gamma_E^{(n)}$ and $\Pi_k^{(n)}$ are changing and the evolution of large scale bias would in principal depends on the specific parameters b_n adopted, since the Γ_E and Π_k evolve with time oppositely. In the examples we shows, $\Gamma_E^{(1)}(k)$ dominates the evolution, i.e. galaxies formed at lower redshift would be higher biased due to the stronger nonlinear effects.

Finally, we consider the continuous galaxy formation model, assuming a simple log-normal model for average galaxy formation rate [11]

$$f(z)=N_g\exp\left[-\frac{[\log(1+z)-\log(1+z_0)]^2}{2\sigma^2}\right], \quad (74)$$

where N_g is the normalization factor ensuring $\int dz f(z)=1$. Therefore, we have two parameters characterizing the model: z_0 the peak redshift of galaxy formation, and σ^2 the width of the redshift for galaxy formation. In the lower panel of Fig.(16), we give several examples of galaxy formation history.

In the left-upper panel of Fig.(16), we present again the normalized propagator for various galaxy formation models which we shows in the lower panel of the same figure. As discussed previously, the $\Gamma_g^{(1)}(k;z_{obs})$ here is simply a time average of $\Gamma_g^{(1)}(k;z_{form},z_{obs})$ weighted with $f(z_{form})$. Therefore, for a narrower formation history (e.g. the dashed, dotted and dash-dotted lines), where $\sigma^2=0.01$, the results are similar to corresponding galaxy bursting models with different z_0. On the other hand, when galaxy tends to form in a similar rate during a longer time (solid and long-dashed lines), e.g. $\sigma^2=0.1$,

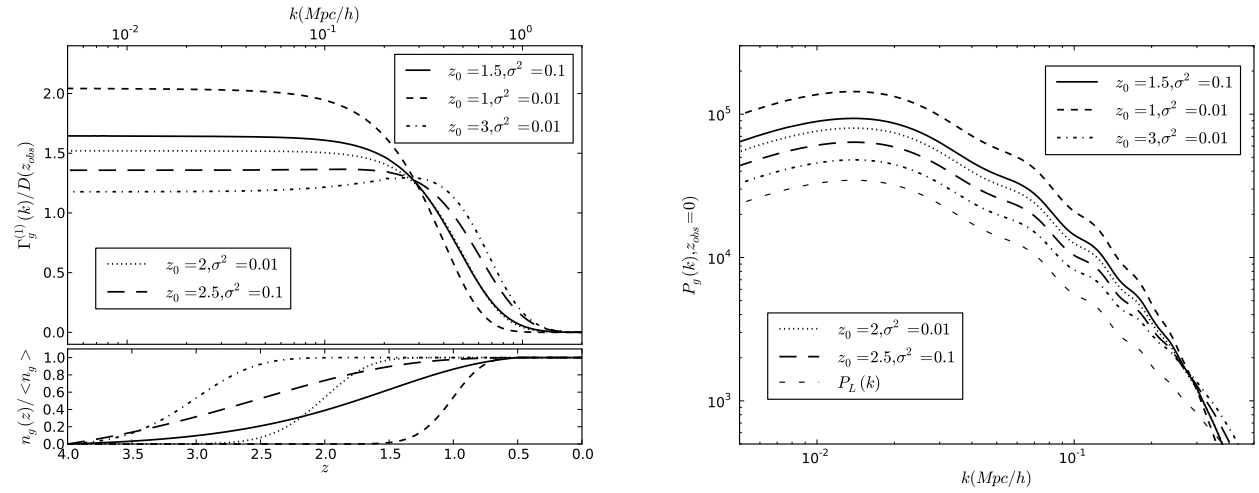

FIG. 16: The normalized two-point propagator (*left*) $\Gamma_g^{(1)}(k;\ z_{form},\ z_{obs})/D(z_{obs})$ and corresponding power spectrum (*right*) for various models with continuous galaxy formation. (*left-lower*): The cumulative average galaxy formation history for models shown in the upper panel.

we are more likely to observe a galaxy power spectrum with medium amplitude and nonlinear damping. We also illustrate the corresponding power spectrum on the right panel of Fig.(16).

VI. CONCLUSION AND DISCUSSION

An accurate modeling of the statistics of galaxy density perturbation is crucial for the success of next generation galaxy surveys. In this paper, we considered the nonlinear bias model in the context of resummed perturbation theory. In Section III, we discussed the Eulerian bias model and then generalized it to incorporate the continuous galaxy formation in Section IV. By utilizing the multipoint propagators of the matter field, our formalism for Eulerian bias model is more accurate than the standard approach in both the linear as well as the quasi-linear regimes. This has already been verified in the work of [16], where a good agreement was achieved comparing to the simulation even for the slowly converging logarithmic mapping of the density distribution. However, a detailed comparison with high-precision simulation is still needed, in at least two different levels: the accuracy of perturbative calculation itself compared to the cost of its numerical calculation, and the ability of describing the scale-dependent galaxy clustering bias at the epoch of their formation.

Furthermore, even after separating out the subsequent gravitational non-locality, the bias parameters could still be nonlocal. For example, the $\Delta\rho$ in Eq. (36) only counts the effective newborn galaxies that finally entered into the sample, however, such description is more or less ambiguous due to galaxy merger. Therefore, the identified progenitors in our formalism then include all merged galaxies, which would introduce a effective non-locality in the functional $F[\delta_m]$. In principle, this could be solved by introducing another merger contributions in the integration, but with the cost that could further complicate the model.

Acknowledgments

XW thanks for the productive discussion with Donghui Jeong, Mark Neyrinck, Patrick McDonald and Kwan Chuen Chan. XW and AS are grateful for support from the Gordon and Betty Moore Foundations.

Appendix A: Matter Density Propagator in Lagrangian Perturbation Theory

Here we consider the generalized multipoint propagator

$$\Pi_k^{(n)}(\mathbf{p}_1,\cdots,\mathbf{p}_n)=\frac{1}{n!}\left\langle\frac{\delta^n\ \widetilde{e^{-i\mathbf{k}\cdot\mathbf{\Psi}}}(\mathbf{p})}{\delta\phi(\mathbf{p}_1)\cdots\delta\phi(\mathbf{p}_n)}\right\rangle \quad \text{(A1)}$$

When $\mathbf{p}_1+\cdots+\mathbf{p}_n=\mathbf{k}$, one retrieves the $(n+1)-$point propagator $\Gamma_m^{(n)}$. For $n=0$, we define $\Pi^{(0)}(\mathbf{k})$ as

$$\Pi^{(0)}(\mathbf{k})=\left\langle e^{-i\mathbf{k}\cdot\mathbf{\Psi}(0)}\right\rangle\approx\exp\left[-\frac{k^2}{6}\langle|\mathbf{\Psi}(0)|^2\rangle\right] \quad \text{(A2)}$$

As shown in Eq.(27).

$$\begin{aligned}\Pi_k^{(1)}(\mathbf{p}) &= \Pi^{(0)}(\mathbf{k})\left\langle\frac{\delta}{\delta\phi(\mathbf{p})}\widetilde{e^{-i\mathbf{k}\cdot\mathbf{\Psi}}}(\mathbf{p})\right\rangle_c\\ &= \Pi^{(0)}(\mathbf{k})\ T^{(1)}(\mathbf{k},\mathbf{p}). \quad \text{(A3)}\end{aligned}$$

We then explicitly expands the terms inside ensemble average, which will be denoted as $T^{(1)}(\mathbf{k})$ in the following

$$T^{(1)}(\mathbf{k},\mathbf{p}) = \sum_{n=0,m=1}^{\infty} \frac{(-i)^n D^m}{n!(m-1)!} \Big\langle \Big[\int d^3\mathbf{q}\ \mathbf{k}\cdot\mathbf{\Psi}(\mathbf{q})\Big]^n \int d^3\mathbf{p}\ d^3\mathbf{p}'_{1\cdots(m-1)} \delta_D(\mathbf{p}-\mathbf{k}-\mathbf{p}'_{1\cdots m-1}) \big[\mathbf{k}\cdot\mathbf{L}^{(m)}(\mathbf{p}'_1, \cdots,\mathbf{p}'_{m-1},\mathbf{k})\big]\ \big[\delta_0(\mathbf{p}'_1)\cdots\delta_0(\mathbf{p}'_{m-1})\big]\Big\rangle_c \quad \text{(A4)}$$

Fig(4) shows all the contributions up to the one-loop order. Denotes $T^{(1)}_{n,m}(\mathbf{k})$ as individual terms been summed in above equation, we have

$$\begin{aligned} T^{(1)}_{0,1} &= D(\eta)k_i L^{(1)}_i, \\ T^{(1)}_{0,3} &= \frac{D^3(\eta)k_i}{2}\int d^3\mathbf{q}\ L^{(3)}_i(\mathbf{q},-\mathbf{q},\mathbf{p})P_0(q) \\ T^{(1)}_{1,2} &= D^3(\eta)k_i k_j \int d^3\mathbf{q}\ L^{(1)}_i(\mathbf{q})L^{(2)}_j(-\mathbf{q},\mathbf{p})P_0(q), \end{aligned} \quad \text{(A5)}$$

where LPT kernel $\mathbf{L}^{(n)}(\mathbf{p}_1,\cdots,\mathbf{p}_n)$

$$\begin{aligned} \mathbf{L}^{(1)} &= \frac{\mathbf{p}}{p^2} \\ \mathbf{L}^{(2)} &= \frac{3}{7}\frac{\mathbf{p}}{p^2}\left[1-\mu^2_{1,2}\right] \\ \mathbf{L}^{(3a)} &= \frac{5}{7}\frac{\mathbf{p}}{p^2}\left[1-\mu^2_{1,2}\right]\left[1-\mu^2_{12,3}\right] - \frac{1}{3}\frac{\mathbf{p}}{p^2}[1-3\mu^2_{1,2} \\ &\quad +2\mu_{1,2}\mu_{2,3}\mu_{3,1}] + \mathbf{p}\times\mathbf{T} \\ \mathbf{L}^{(3)} &= \frac{1}{3}[\mathbf{L}^{(3a)} + perm] \end{aligned} \quad \text{(A6)}$$

Substituting the definition of $\mathbf{L}^{(n)}(\mathbf{p}_1,\cdots,\mathbf{p}_n)$ into Eq.(A4), one can explicit carry out $T^{(1)}$ up to the one-loop order,

$$\begin{aligned} T^{(1)}_{0,1} &= D(\eta)\frac{k_i p_i}{p^2} \\ T^{(1)}_{0,3} &= \frac{5}{21}D^3(\eta)\frac{k_i p_i}{p^2}R_1(p) \\ T^{(1)}_{1,2} &= \frac{3}{14}D^3(\eta)\Big[\left(\frac{\mathbf{k}\cdot\mathbf{p}}{p^2}\right)^2[R_1(p)+2R_2(p)] \\ &\quad -\frac{k^2}{p^2}R_1(p)\Big] \end{aligned} \quad \text{(A7)}$$

where we have defined a slightly different version of the integral functions $R_n(k)$ introduced by [4] Here we denotes

$$R_n(k) = \frac{1}{48}\frac{k^3}{4\pi^2}\int_0^\infty dr\ P_0(kr)\tilde{R}_n. \quad \text{(A8)}$$

and

$$\begin{aligned} \tilde{R}_1 &= -\frac{2}{r^2}(1+r^2)(3-14r^2+3r^4) \\ &\quad +\frac{3}{r^3}(r^2-1)\ln\left|\frac{1+r}{1-r}\right| \\ \tilde{R}_2 &= \frac{2}{r^2}(1-r^2)(3-2r^2+3r^4) \\ &\quad +\ \frac{3}{r^3}(r^2-1)^3(1+r^2)\ln\left|\frac{1+r}{1-r}\right| \end{aligned} \quad \text{(A9)}$$

Setting $\mathbf{k}=\mathbf{p}$ in Eq. (A7), we get the $T^{(1)}(k)$ up to one-loop order

$$\begin{aligned} T^{(1)}_{\rm tree} &= D(\eta) \\ T^{(1)}_{1-{\rm loop}}(k) &= D(\eta)^3\int\frac{d^3\mathbf{p}}{504k^3p^5}P_L(p)\Big[6k^7p+5k^5p^3+50k^3p^5 \\ &\quad -21kp^7+\frac{3}{2}(k^2-p^2)^3(2k^2+7p^2)\ln\left|\frac{k-p}{k+p}\right|\Big]. \end{aligned} \quad \text{(A10)}$$

which coincide with the calculation of [20]. For three-point $\Pi^{(2)}_k(\mathbf{p}_1,\mathbf{p}_2)$

$$\begin{aligned} \Pi^{(2)}_k(\mathbf{p}_1,\mathbf{p}_2) &= \frac{1}{2}\Pi^{(0)}(k)\left\langle\frac{\delta^2}{\delta\phi(\mathbf{p}_1)\delta\phi(\mathbf{p}_2)}\widetilde{e^{-i\mathbf{k}\cdot\mathbf{\Psi}}}(\mathbf{p})\right\rangle_c \\ &\approx \Pi^{(0)}(k)\frac{D^2(\eta)}{2}\Big[k_iL^{(2)}_i(\mathbf{p}_1,\mathbf{p}_2)+ \\ &\quad +\ k_ik_jL^{(1)}_i(\mathbf{p}_1)L^{(1)}_i(\mathbf{p}_2)\Big] \end{aligned} \quad \text{(A11)}$$

Assuming $\mathbf{k}=\mathbf{p}_1+\mathbf{p}_2$, One recover the tree-level result $\Gamma^{(2)}_m(\mathbf{k})$,

$$\Gamma^{(2)}_m(\mathbf{k}_1,\mathbf{k}_2) = \Pi^{(0)}(\mathbf{k})F_2(\mathbf{k}_1,\mathbf{k}_2), \quad \text{(A12)}$$

where F_2 is the second order Eulerian perturbation kernel.

Appendix B: Two-loop Order of $\Gamma^{(1)}_E$

In this paper, we have calculated the two-point propagator $\Gamma^{(1)}_E$ up to two-loop order. Seven non-vanishing contributions are depicted in Fig.(17). From these diagrams, one can write down all terms explicitly

$$\Gamma^{(1,\ 2{\rm lp})}_{E,\ a}(\mathbf{k};\eta) = \int d^3\mathbf{p}_{12}\ P_0(p_1)P_0(p_2)\ \left[\sum_{i=1}^{7}\ \mathcal{K}^{(1,\ 2{\rm lp})}_i\right] \quad \text{(B1)}$$

where

$$\begin{aligned} \mathcal{K}^{(1,\ 2{\rm lp})}_1 &= 6\ b_2(\mathbf{k}+\mathbf{p}_1+\mathbf{p}_2,-\mathbf{p}_1-\mathbf{p}_2)\ \Gamma^{(2)}_m(-\mathbf{p}_1,-\mathbf{p}_2;R) \\ &\quad \times\ \Gamma^{(3)}_{m,\ a}(\mathbf{k},\mathbf{p}_1,\mathbf{p}_2;R), \end{aligned}$$

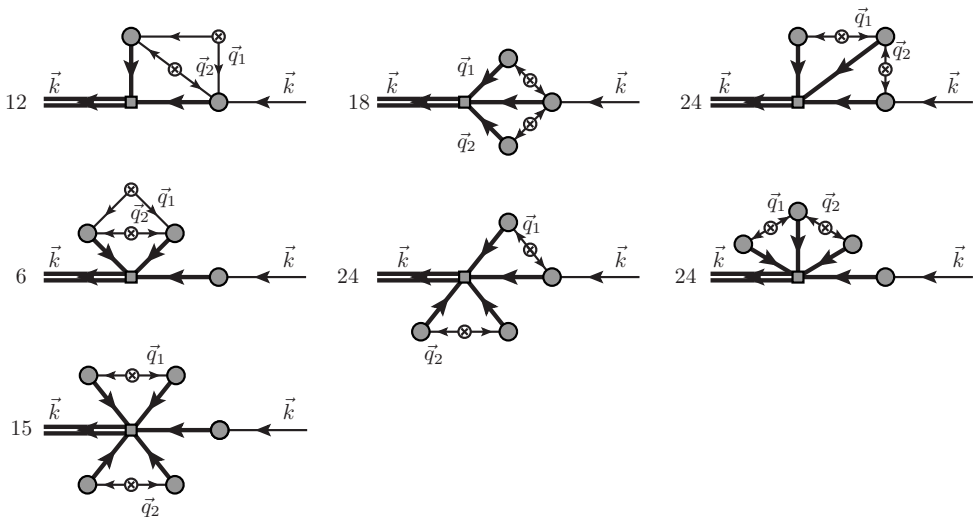

FIG. 17: Two-loop order of the two-point nonlinear propagator.

$$\mathcal{K}_2^{(1,\ 2\mathrm{lp})} = 3\ b_3(\mathbf{k}+\mathbf{p}_1+\mathbf{p}_2,-\mathbf{p}_1,-\mathbf{p}_2)\Gamma^{(3)}_{m,\ a}(\mathbf{k},\mathbf{p}_1,\mathbf{p}_2;R) \times \Gamma^{(1)}_m(-\mathbf{p}_1;R)\Gamma^{(1)}_m(-\mathbf{p}_2;R),$$

$$\mathcal{K}_3^{(1,\ 2\mathrm{lp})} = 4\ b_3(\mathbf{k}-\mathbf{p}_2,\mathbf{p}_1+\mathbf{p}_2,-\mathbf{p}_1)\ \Gamma^{(2)}_m(\mathbf{p}_1,\mathbf{p}_2;R) \times \Gamma^{(1)}_m(-\mathbf{p}_1;R)\Gamma^{(2)}_{m,\ a}(\mathbf{k},-\mathbf{p}_2;R)$$

$$\mathcal{K}_4^{(1,\ 2\mathrm{lp})} = b_3(\mathbf{k},\mathbf{p}_1+\mathbf{p}_2,-\mathbf{p}_1-\mathbf{p}_2)\ \Gamma^{(2)}_m(\mathbf{p}_1,\mathbf{p}_2;R) \times \Gamma^{(2)}_m(-\mathbf{p}_1,-\mathbf{p}_2;R)\Gamma^{(1)}_{m,\ a}(\mathbf{k};R)$$

$$\mathcal{K}_5^{(1,\ 2\mathrm{lp})} = b_4(\mathbf{k}-\mathbf{p}_1,\mathbf{p}_2,-\mathbf{p}_2,-\mathbf{p}_1)\ \left[\Gamma^{(1)}_m(\mathbf{p}_2;R)\right]^2 \times \Gamma^{(1)}_m(\mathbf{p}_1;R)\Gamma^{(2)}_{m,\ a}(\mathbf{k},-\mathbf{p}_1;R)$$

$$\mathcal{K}_6^{(1,\ 2\mathrm{lp})} = b_4(\mathbf{k},\mathbf{p}_1+\mathbf{p}_2,-\mathbf{p}_1,-\mathbf{p}_2)\ \Gamma^{(2)}_m(\mathbf{p}_1,\mathbf{p}_2;R) \times \Gamma^{(1)}_m(-\mathbf{p}_1;R)\Gamma^{(1)}_m(-\mathbf{p}_2;R)\Gamma^{(1)}_{m,\ a}(\mathbf{k};R)$$

$$\mathcal{K}_7^{(1,\ 2\mathrm{lp})} = \frac{1}{8}\ b_5(\mathbf{k},\mathbf{p}_1,-\mathbf{p}_1,\mathbf{p}_2,-\mathbf{p}_2)\left[\Gamma^{(1)}_m(\mathbf{p}_1;R)\right]^2 \times \left[\Gamma^{(1)}_m(\mathbf{p}_2;R)\right]^2\Gamma^{(1)}_{m,\ a}(\mathbf{k};R) \qquad \text{(B2)}$$

Appendix C: One-loop Order of $\Gamma_E^{(2)}$

At one-loop level, five diagrams are nonzero.

$$\Gamma^{(2,\ 1\mathrm{lp})}_{E,\ ab}(\mathbf{p},\mathbf{k}-\mathbf{p};\eta) = \int d^3\mathbf{p}\ P_0(q)\ \left[\sum_{i=1}^{5}\ \mathcal{K}_i^{(2,\ 1\mathrm{lp})}\right]. \qquad \text{(C1)}$$

where

$$\mathcal{K}_1^{(2,\ 1\mathrm{lp})} = 3\ b_2(\mathbf{k}+\mathbf{q},-\mathbf{q})\Gamma^{(3)}_{m,\ ab}(\mathbf{k}-\mathbf{p},\mathbf{p},\mathbf{q};R) \times\ \Gamma^{(1)}_m(-\mathbf{q};R)$$

$$\mathcal{K}_2^{(2,\ 1\mathrm{lp})} = 2\ b_2(\mathbf{k}-\mathbf{p}-\mathbf{q},\mathbf{p}+\mathbf{q})\ \ \Gamma^{(2)}_{m,\ a}(\mathbf{p},\mathbf{q};R) \times \Gamma^{(2)}_{m,\ b}(\mathbf{k}-\mathbf{p},-\mathbf{q};R)$$

$$\mathcal{K}_3^{(2,\ 1\mathrm{lp})} = 2\ b_3(\mathbf{k}-\mathbf{p},\mathbf{p}+\mathbf{q},-\mathbf{q})\ \ \Gamma^{(1)}_m(\mathbf{q};R) \times \Gamma^{(1)}_{m,\ a}(\mathbf{k}-\mathbf{p};R)\Gamma^{(2)}_{m,\ b}(\mathbf{p},\mathbf{q};R)$$

$$\mathcal{K}_4^{(2,\ 1\mathrm{lp})} = \frac{1}{2}\ b_3(\mathbf{k},\mathbf{q},-\mathbf{q})\ \Gamma^{(2)}_{m,\ ab}(\mathbf{p},\mathbf{k}-\mathbf{p};R) \times \left[\Gamma^{(1)}_m(\mathbf{q};R)\right]^2$$

$$\mathcal{K}_5^{(2,\ 1\mathrm{lp})} = \frac{1}{4}\ b_4(\mathbf{k}-\mathbf{p},\mathbf{p},\mathbf{q},-\mathbf{q})\ \Gamma^{(1)}_{m,\ a}(\mathbf{k}-\mathbf{q};R) \times\ \left[\Gamma^{(1)}_m(\mathbf{q};R)\right]^2\Gamma^{(1)}_{m,\ b}(\mathbf{p};R). \qquad \text{(C2)}$$

In Eq.(C2), $\mathcal{K}_1$ and $\mathcal{K}_2$ are two-Ξ_m contributions from the first and second terms of Eq.(55) respectively, $\mathcal{K}_3$ and $\mathcal{K}_4$ are three-Ξ_m contributions, and $\mathcal{K}_5$ is the four-Ξ_m contribution.

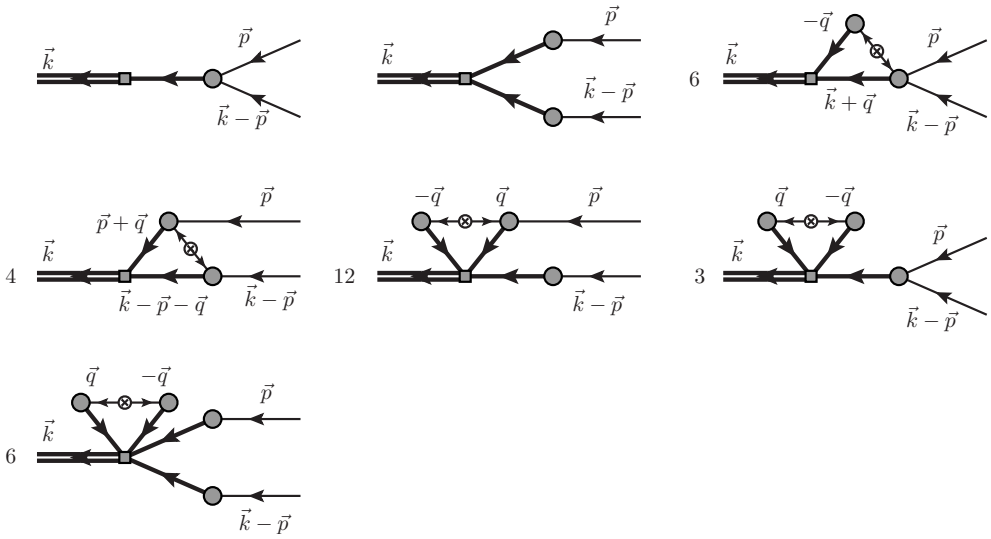

FIG. 18: Three-point nonlinear propagator $\Gamma_E^{(2)}$ up to one-loop order.

[1] M. Crocce and R. Scoccimarro, Phys. Rev. D **73**, 063519 (2006)
[2] M. Crocce and R. Scoccimarro, Phys. Rev. D **73**, 063520 (2006)
[3] F. Bernardeau, M. Crocce and R. Scoccimarro, Phys. Rev. D **78**, 103521 (2008)
[4] T. Matsubara, Phys. Rev. D **77**, 063530 (2008)
[5] A. Taruya and T. Hiramatsu, Astrophys. J. **674**, 617 (2008)
[6] M. Pietroni, JCAP **0810**, 036 (2008)
[7] A. G. Sanchez and S. Cole, Mon. Not. Roy. Astron. Soc. **385**, 830 (2008)
[8] W. J. Percival, R. C. Nichol, D. J. Eisenstein, J. A. Frieman, M. Fukugita, J. Loveday, A. C. Pope and D. P. Schneider *et al.*, Astrophys. J. **657**, 645 (2007)
[9] S. Cole *et al.* [The 2dFGRS Collaboration], Mon. Not. Roy. Astron. Soc. **362**, 505 (2005)
[10] T. Matsubara, Phys. Rev. D **83**, 083518 (2011)
[11] K. C. Chan, R. Scoccimarro and R. K. Sheth, arXiv:1201.3614 [astro-ph.CO].
[12] T. Matsubara, Phys. Rev. D **78**, 083519 (2008) [Erratum-ibid. D **78**, 109901 (2008)]
[13] A. Elia, S. Kulkarni, C. Porciani, M. Pietroni and S. Matarrese, Mon. Not. Roy. Astron. Soc. **416**, 1703 (2011)
[14] P. McDonald, Phys. Rev. D **74**, 103512 (2006) [Erratum-ibid. D **74**, 129901 (2006)]
[15] P. McDonald and A. Roy, JCAP **0908**, 020 (2009)
[16] X. Wang, M. Neyrinck, I. Szapudi, A. Szalay, X. Chen, J. Lesgourgues, A. Riotto and M. Sloth, Astrophys. J. **735**, 32 (2011)
[17] R. J. Scherrer and D. H. Weinberg, Astrophys. J. **504**, 607 (1998)
[18] M. Tegmark and P. J. E. Peebles, Astrophys. J. **500**, L79 (2011)
[19] D. J. Eisenstein and W. Hu, Astrophys. J. **496**, 605 (1998)
[20] F. Bernardeau, M. Crocce and R. Scoccimarro, arXiv:1112.3895 [astro-ph.CO].